Marine and Petroleum Geology 145 (2022) 105885

Contents lists available at ScienceDirect

Marine and Petroleum Geology

journal homepage: www.elsevier.com/locate/marpetgeo

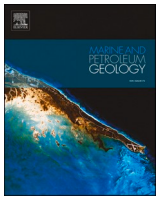

An integrated petrographical, petrophysical and organic geochemical characterization of the Lower Turonian Abu Roash-F carbonates, Abu Gharadig field, Egypt – Inferences on self-sourced unconventional reservoir potential

Sherif Farouk [a], Souvik Sen [b,*,1], Shib Sankar Ganguli [c], Fayez Ahmad [d], Mohamed Abioui [e], Khaled Al-Kahtany [f], Priyantan Gupta [g]

[a] Exploration Department, Egyptian Petroleum Research Institute (EPRI), 1 Ahmed El-Zomor Street, Nasr City, Cairo, Egypt
[b] Geologix Limited, Dynasty Building, Wing A, Level 4, Andheri Kurla Road, Andheri (E), Mumbai, 400059, Maharashtra, India
[c] Marine & Deep Seismics Research Group, CSIR-National Geophysical Research Institute, Uppal Road, Hyderabad, 500007, Telangana State, India
[d] Department of Earth and Environmental Sciences, Prince EL-Hassan Bin Talal Faculty for Natural Resources and Environment, The Hashemite University, Zarqa, Jordan
[e] Department of Earth Sciences, Faculty of Sciences, Ibn Zohr University, Agadir, Morocco
[f] Geology and Geophysics Department, College of Science, King Saud University, Riyadh, Saudi Arabia
[g] Department of Geology and Geophysics, Indian Institute of Technology Kharagpur, West Bengal, 721302, India

ARTICLE INFO

Keywords:
Petrography
Microfacies
Carbonate source rock
Reservoir quality
Unconventional
Abu roash F Member
Western desert

ABSTRACT

Marine carbonate source rocks are ubiquitous worldwide and many of these can act as self-sourced unconventional reservoirs. This work focuses on the Lower Turonian Abu Roash-F Member from the prolific Abu Gharadig field, Western Desert, Egypt which consists of argillaceous and bioclastic limestones. Thin section petrographic analysis indicated the presence of various microfacies assemblages dominated by planktonic foraminifera in association with abundant calcispheres indicating an open-marine, deep-shelf depositional setting. The X-Ray Fluorescence data exhibits overall poor detrital influx throughout the AR-F while the Mo and V enrichment in the lower part represents Late Cenomanian/Early Turonian (C/T) oceanic anoxic event (OAE2) associated with the global sea-level rise. Geochemical analysis suggests that the studied AR-F has good to very good total organic carbon (TOC) content (up to 3.57 wt%) consists of Type-II kerogen (HI > 400 mgHC/gTOC), thermally mature (T_{max} ~ 438.5 °C) and presently within the oil generation window. The TOC-rich (>2.5 wt%), highly anoxic lower AR-F showed higher oil production probability which is inferred as a sweet spot zone. Petrophysically AR-F is very tight and impervious with 0.9–2.6% porosity and negligible permeability (<0.0033 mD), dominated by nano- and microporosities. Micritization is found to be the most dominant diagenetic process reducing the AR-F storage capacity, followed by calcite cementation filling the bioclast tests and fractures, chemical compaction (stylolites), and minor dolomitization. 2D CT scanning revealed some minor vuggy or fracture pores but those were isolated and lacks in connectivity, which therefore did not improve the flow capacity of AR-F. Therefore, stimulation is necessary to bring this tight carbonate reservoir into production. This study offers critical insights on the AR-F Member which is an excellent source rock and at the same time holds potential as a promising unconventional reservoir.

1. Introduction

Unconventional hydrocarbon reservoirs are extensively studied and reported, especially from the North American basins, and a majority of those are shale reservoirs (Bryndzia and Braunsdorf, 2014). However, self-sourced non-shale hydrocarbon reservoirs are less reported globally.

* Corresponding author.
E-mail addresses: geo.sherif@hotmail.com (S. Farouk), souvikseniitb@gmail.com (S. Sen), ganguli.ism@gmail.com (S.S. Ganguli), fayezahmad3@hotmail.com (F. Ahmad), m.abioui@uiz.ac.ma, abioui.gbs@gmail.com (M. Abioui), km2007_khld@yahoo.com (K. Al-Kahtany), priyantan1997@gmail.com (P. Gupta).
[1] Present affiliation: Halliburton Consulting, Mumbai-400063, Maharashtra, India.

https://doi.org/10.1016/j.marpetgeo.2022.105885
Received 23 January 2022; Received in revised form 16 August 2022; Accepted 18 August 2022
Available online 24 August 2022
0264-8172/© 2022 Elsevier Ltd. All rights reserved.

One of the most famous unconventional reservoirs is the Eagle Ford Formation (USA), which is not strictly a shale, rather marl/lime mud consisting of fossiliferous carbonate material (up to 90 wt%) with some fraction of biosiliceous radiolarian tests and sponge spicules (Ozkan et al., 2013) that exhibits 2–6 wt% TOC (Bryndzia and Braunsdorf, 2014). There have been a few examples of self-generating and self-storing carbonates globally. Wei et al. (2017) interpreted the Ordovician Majiagou Formation of the Ordos Basin (China) as one of such types of reservoirs which consists of marine mud flat carbonate deposits (argillaceous dolomite and dolomitic mudstone) with 1–5 wt% TOC. Chen et al. (2020) briefly interpreted the source rock qualities of the low TOC Middle-Upper Ordovician limestones in Tarim Basin (China) and interpreted that the effective source rock is also a potential self-sourced and self-retained unconventional reservoir system. Radwan et al. (2021) interpreted the Eocene carbonates of the Radwany Formation (Egypt) which exhibit similar characteristics with the TOC range of about 1.22–6 wt%. These are petrophysically tight, yielding an organic-rich potential unconventional reservoir. Another recent work by Boutaleb et al. (2021) showed the Lower Turonian deep marine carbonates from the SE Constantine field (Algeria) are mainly organic-rich tight limestone and dolostones that were deposited during oceanic anoxia and have excellent unconventional resource potential. In general, TOC-rich carbonates have been reported to be tight and petrophysically inferior but can be an excellent self-sourced unconventional reservoir.

In this work, we focused on the Lower Turonian Abu Roash-F (AR-F) carbonates of the Abu Gharadig field which is a massive hydrocarbon-bearing field situated in the central part of the prolific Abu Gharadig Basin (AGB) of the Western Desert (El Gazzar et al., 2016). The field is primarily produced from the Cenomanian Bahariya Formation, Upper Turonian AR-C, AR-D and AR-E members and Bahariya Formation (Hewaidy et al., 2018; Farouk et al., 2022). Researchers have worked on AR-F from various parts of the Western Desert (e.g., Awad, 1984; Bayoumi and Lotfy, 1989; Abdel-Kireem et al., 1996; Hantar, 1990; El Sherbiny, 2002; El Beialy et al., 2010; El Atfy, 2011; Zobaa et al., 2011; El Diasty, 2014; Makky et al., 2014; Adly et al., 2016; Ghassal et al., 2018; Sarhan and Basal, 2020; Yang, 2020 and others) and interpreted that AR-F is a prominent source rock deposited in a marine environment (possibly shallow marine). Zobaa et al. (2011) linked the organic-rich AR-F intervals with the Turonian-Cenomanian oceanic anoxia event which prevailed throughout North Africa during a major global sea-level rise (Herbin et al., 1986; Klemme and Ulmishek, 1991; Lüning et al., 2004; Zobaa et al., 2009).

Apart from the organic geochemical aspects, detailed formation characteristics of AR-F are lacking in the literature, which sets the premise of this work. Petrographic and petrophysical characterization along with the understanding of diagenetic effects are critical to understanding the potential of AR-F as an unconventional reservoir. The primary objectives of this work are to: i) identify various lithofacies and microfacies and infer depositional environment, ii) interpret key petrophysical properties to assess reservoir quality parameters, and iii) assess source rock geochemical characteristics.

We have integrated thin sections, computed tomography (CT) scan and scanning electron microscopy (SEM) images, routine core analysis, X-Ray Fluorescence (XRF) data, Rock-Eval pyrolysis, mudlog data, and a suite of wireline logs to achieve these objectives. Based on the results, we have drawn inferences on the self-sourced unconventional reservoir potential of the proven source rock AR-F Member in the Abu Gharadig field. The work is timely and important given the fact that the operators in the Western Desert are looking beyond the proven conventional reservoirs (AR-G Member, Bahariya Formation, etc.) to increase the resource base. Recently, the tight carbonates of the AR-D Member have been stimulated successfully and put into production, which was otherwise excluded from the completion. These approaches are critically important to increase the domestic hydrocarbon production from existing fields using the facilities and infrastructures already in place.

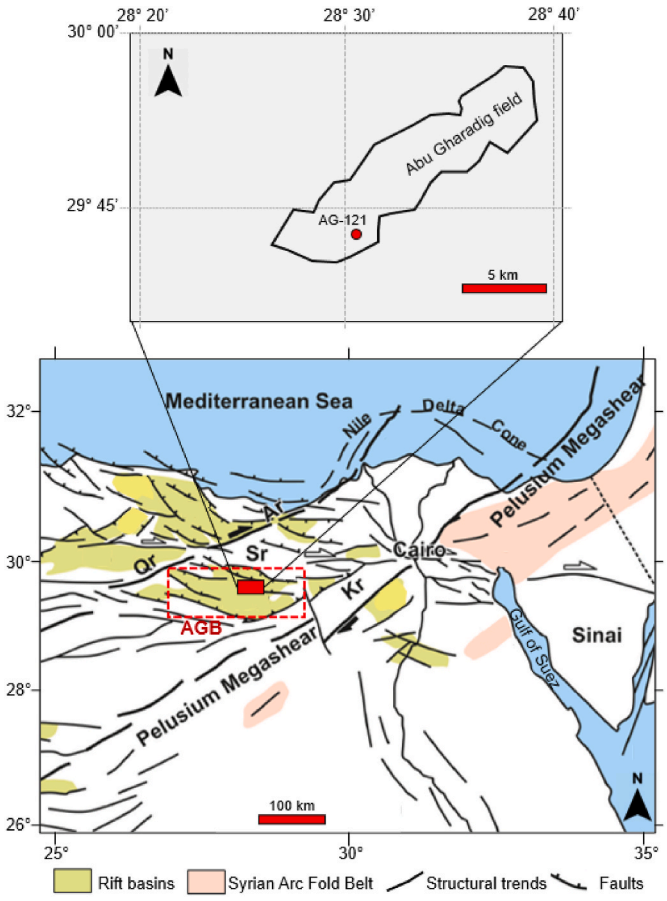

Fig. 1. Location Map of the study area and studied well within Abu Gharadig Basin (AGB) in the Western Desert along with the major structural features (Qr = Qattara Ridge, Sr = Sharib-Sheiba Ridge, Kr = Kattaniya Ridge), adapted from Shalaby and Sarhan (2021).

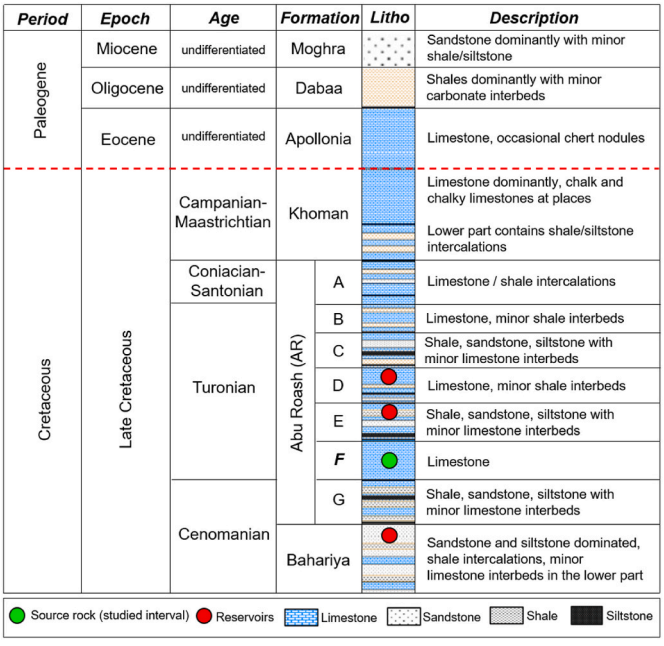

Fig. 2. Stratigraphic column of the Abu Gharadig Basin, Western Desert, modified after Shalaby and Sarhan (2021).

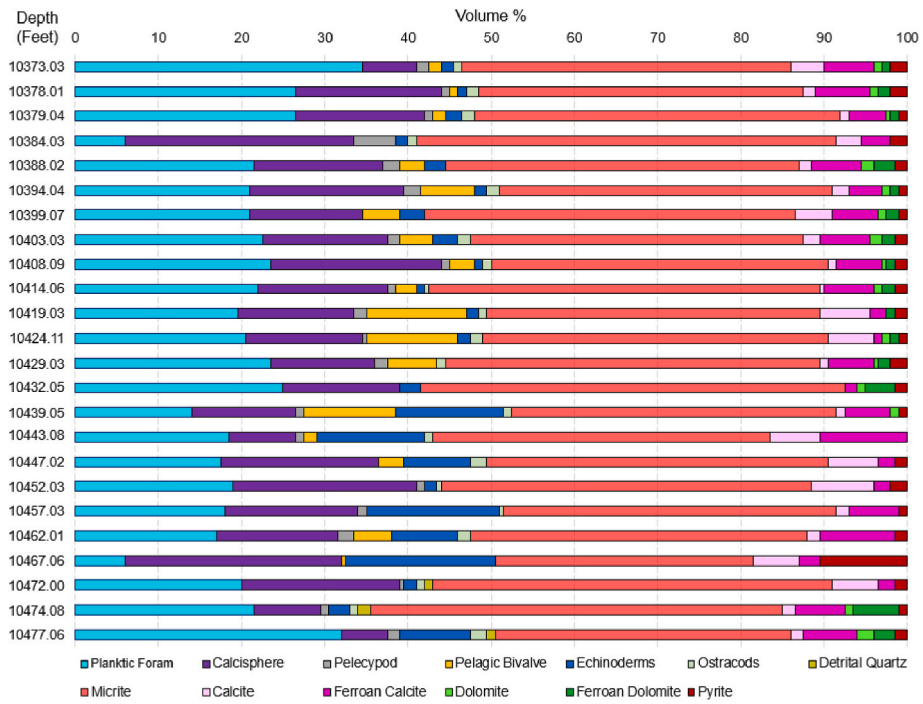

Fig. 3. Relative abundances of the major components (in % by volume) within the AR-F Member, as observed in well AG-121.

2. Geological setting

The Abu Gharadig Basin (AGB) is an elliptical-shaped E-W trending intra-cratonic Mesozoic rift basin situated in the Northwestern Desert of Egypt (El Gazzar et al., 2016). The Qattara Ridge and Sharib-Sheiba Ridge separate it from the northern rift basins while the Kattaniya Ridge marks its southern and southeastern boundary (Farouk et al., 2021). The location map of the AGB is illustrated in Fig. 1. The Late Jurassic to Early Cretaceous rifting created various E-W and ENE-WSW trending half grabens including the AGB along the Northern African margin and within the intraplate region (Guiraud and Maurin, 1992). The rifting ceased during the Late Cretaceous and the basin experienced a NW-SE compression (during the Alpine orogeny), which continued throughout the Tertiary period (Moustafa, 2008; Sarhan, 2017a-c). Bosworth et al. (2008) interpreted that the northern part of the AGB experienced the majority of the shortening. The tilting and basin inversion was responsible for creating the major structural traps in the western desert (Sarhan and Collier, 2018). Moustafa (2013) interpreted that AGB anticlinal traps might be formed due to the rifting-related subsidence.

The studied Abu Gharadig field is the first massive hydrocarbon discovery from the central part of the AGB (El Gazzar et al., 2016). It is situated between 28.2 °E−28.5 °E and 29.35 °N-30 °N. The field covers roughly 60 km^2 area and hosts roughly 12,000 feet of mixed siliciclastic and carbonate sediments of the Cretaceous to Paleogene age. A regional stratigraphic sequence is presented in Fig. 2 (Shalaby and Sarhan, 2021). A regional unconformity marks the boundary between the Paleogene and Mesozoic strata. The post-rift sediments of the Late Cretaceous age represent major transgressive cycles with minor interruptions by shorter regressive cycles. The Abu Roash (AR) Formation is subdivided into seven distinct members, marked as A-G. Researchers have interpreted that the AR-F limestones are the main source rock of the ABG (Adly et al., 2016; Ghassal et al., 2018). The Cenomanian Bahariya, Upper Turonian AR-C, and AR-E formations are the primary reservoirs of the Abu Gharadig field. Both these formations are dominated by sandstone, siltstone, and shale intercalations along with occasional limestones. The AR-D member, mainly limestone-dominated along with minor shale interbeds equally possesses reservoir potential. On the contrary, the AR-E consists of both clastics and carbonates.

3. Materials and methods

In this work, we analyzed a vertical well named AG-121 which is drilled up to a depth of 12,123 feet in 2014. A cumulative of 110 feet core was recovered from the Lower Turonian AR-F Formation (10,370-10480 feet) in the studied well. A total of 24 thin sections were examined under plane- and cross-polarized light with a petrographic polarizing microscope. The texture, mineralogy and porosity of each thin section were described and the relative abundances (in % by volume) of all components were determined by point counting (200 points for each sample). Scanning electron microscope (SEM) analysis was performed to identify and focus on the micro-pores throughout the analyzed samples. The analyzed carbonate samples were petrographically classified according to the Dunham (1962) classification scheme. Identified microfacies types were compared with standard microfacies types and the representative analog scheme presented in Flügel (2010). In addition, diagenetic features were inferred from the studied samples.

We have used routine core analysis (RCAL) data from 26 core plug samples for the petrophysical characterization of the potential reservoir intervals. RCAL provided porosity data acquired by helium porosimeter, and horizontal permeability determined by permeameter. To assess the formation's hydraulic flow properties, we employed the methodology provided by Amaefule et al. (1993) which estimates the reservoir quality index (RQI), normalized porosity index (NPI), and flow zone indicator (FZI) from core-measured porosity and permeability. Pore throat radius was estimated by the Windland equation (Winland, 1972; Kolodzie, 1980). This is a good proxy in absence of the Mercury Injection Capillary Pressure (MICP) test and works well for both the clastics and carbonates (Abuamarah and Nabawy, 2021). 2D CT scanning was performed on the cores to analyze the presence of fractures within the AR-F Member.

Source rock properties were determined by TOC and Rock-Eval pyrolysis data of 22 samples. TOC was determined using the Leco C230 system. A Rock-Eval 6 Pyrolizer was used to analyze free hydrocarbon (S1), remaining HC generation potential (S2), the proportion of CO2 generated from kerogen pyrolysis (S3), and maximum S2 generation temperature (Tmax). Hydrogen Index (HI), Oxygen Index (HI), and

Production Index (PI) have also been derived from arbitrating of organic matter richness based on Peters and Cassa (1994). Trace-element concentrations were determined by handheld X-Ray Fluorescence (XRF) instrument by Thermo Fisher Scientific and the elemental abundances are reported as weight percent (wt%) or parts per million (ppm). XRF data was recorded every foot between 10,370-10482 feet generating 113 data points which were utilized to understand the depositional environment and environmental conditions based on various well-accepted proxies. To understand the reservoir development aspects by hydraulic fracturing, rock-elastic properties and brittleness index of the AR-F were estimated. Poisson's ratio (υ) and Young's modulus (E) were estimated from bulk-density (ρb), compressional (Vp) and shear velocity (Vs):

$$\nu = \frac{Vp^2 - 2Vs^2}{2(Vp^2 - Vs^2)} \quad (1)$$

$$E = \rho b \; Vs^2 \left[\frac{3Vp^2 - 4Vs^2}{Vp^2 - Vs^2}\right] \quad (2)$$

Brittleness index (BI) was calculated using Grieser and Bray's (2007) model, which is based on dynamic elastic properties:

$$BI = \frac{1}{2}\left[\frac{E - Emin}{Emax - Emin} + \frac{\nu - \nu min}{\nu max - \nu min}\right] \quad (3)$$

where υmin and υmax are minimum and maximum Poisson's ratio values respectively, as seen in the AR-F. Similarly, Emin and Emax denote the minimum and maximum Young's modulus, respectively. The BI interpretation guideline by Perez Altamar and Marfurt (2014) suggests that highly ductile rocks have BI < 0.16, moderately ductile rocks have 0.16 < BI < 0.32, and moderately brittle rocks have 0.32 < BI < 0.48, while BI > 0.48 signifies highly brittle rocks. Highly brittle rocks are more responsive to hydraulic fracturing and hence favorable (Nobakht et al., 2013; Ganguli et al., 2021).

4. Results and interpretation

4.1. Lithofacies and microfacies distribution

We have identified two distinct lithofacies within the AR-F Member, and these are: i) argillaceous limestone (AL), and ii) bioclastic limestone (BL). The petrographic analysis allowed the characterization of its texture and composition. The main constituents of these samples can be distinguished into skeletal grains, non-skeletal grains, matrix and types of cement/replacements. The relative abundances of these components (in % by volume) are presented in Fig. 3.

The skeletal grains consist of planktic foraminifera, calcispheres, pelecypods, pelagic bivalves, echinoderms, ostracods, and minor gastropods. Planktic foraminifera is very commonly observed with relative abundances ranging between 6% and 35% by volume. Foram tests are filled with various types of cement including calcite, ferroan calcite, dolomite, ferroan dolomite, kaolinite, secondary silica, and pyrite. The next abundant skeletal grain is observed to be calcispheres with relative abundances ranging between 4 and 24% by volume. Calcispheres are small-sized, hollow spherical and ovoid microfossils exhibiting calcitic walls. Calcispheres tests are mainly filled with calcite and ferroan calcite. Pelecypod shell fragments are recorded in most of the analyzed samples; where it occurs with relative abundances between 0.5% and 5% by volume. They are mainly represented by longitudinal fragments. Thin-shelled pelagic bivalves (filaments) are present in all samples, with relative abundances varying between 0.5% and 12% by volume. Echinoderm fragments are recorded in all (except one sample at depth 10429.03 ft), where it occurs with relative abundances covering 1% up to 16% by volume. The echinoderms are dominated by crinoid arm plates and echinoid spines. Ostracods are recorded in most of the analyzed samples, with relative abundances between 0.5% and 2% by volume. Traces of gastropods are locally observed in only three samples, at depths 10373.03, 10378.01, and 10403.03 ft. Detrital quartz is observed as non-skeletal grains in three samples, at 10472.00, 10474.08 and 10477.06 ft depths, with relative abundances ranging between 1 and 2% by volume.

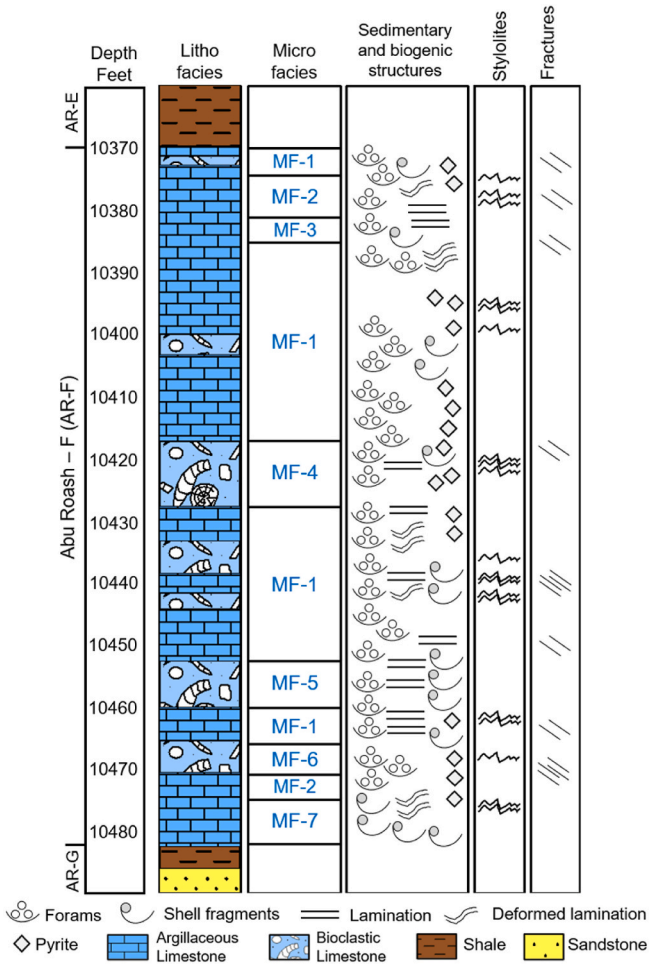

Fig. 4. Lithofacies and microfacies distribution within the AR-F Member of well AG-121.

Micrite matrix is dominantly present in all samples, ranging between 31 and 50.5% by volume. Five types of cements and replacements are observed. Calcite cement is present in all samples (except one sample at a depth of 10432.05 ft), and range in abundances between 0.5 and 7.5% by volume. It is mainly filling bioclast tests and fractures. Ferroan calcite crystals are observed mainly as filling bioclast tests and fractures with relative abundances between 1% and 10.5% by volume. Rare amounts of dolomite are recognized in most of the samples, with relative abundances between trace amounts and 2% by volume. It occurs as euhedral rhombs that are scattered throughout the matrix (reflecting the dolomitization process of limestone) and some are filling bioclast chambers. Ferroan dolomite is present in most of the analyzed samples, where it occurs with relative abundances between trace amounts and 5.5% by volume. It occurs as filling bioclast tests and is scattered throughout the matrix. Pyrite is present in all of the analyzed samples (except one sample at a depth of 10443.08 ft); where it occurs with relative abundances ranging between 1% and 10.5% by volume. It occurs as framboids, and euhedral crystals disseminated throughout the matrix, partially to extensively replace the outer margins of bioclasts or partially to completely fill the foraminiferal tests.

Based on the skeletal and non-skeletal grains, matrix as well as petrographic characteristics, we have identified a total of seven microfacies. These are: i) Muddy allochem limestone (MF-1), ii)

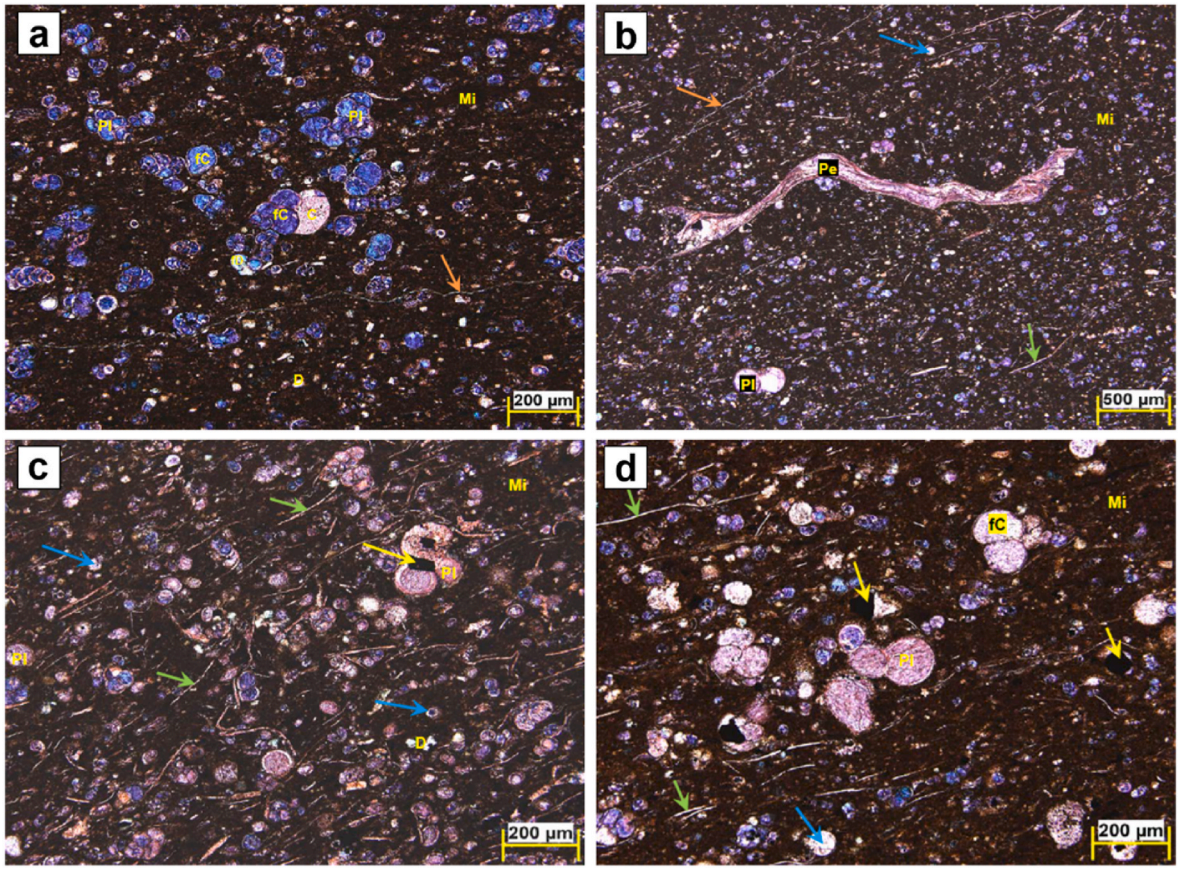

Fig. 5. Thin section photographs of the microfacies MF-1 under plane-polarized light (PPL) at (a) 10373.03 ft, (b) 10388.02 ft, (c) 10394.04 ft, and (d) 10399.07 ft; indicating the presence of micritic matrix (Mi), planktic forams (Pl), hollow spherical and elliptical calcispheres (blue arrows), black pyrite crystals (yellow arrows), echinoderms (E), very few quantities of thin-shelled pelagic bivalves (green arrows), dolomite (D), ferroan calcite (fC; filling bioclastic tests). Orange arrow indicates fracture porosity. (For interpretation of the references to colour in this figure legend, the reader is referred to the Web version of this article.)

Calcispheres and planktic forams wackestone/packstone (LF-2), iii) Calcispheres wackestone/packstone (MF-3), iv) Calcispheres, pelagic bivalves and planktic forams packstone (MF-4), v) Echinoderms, calcispheres and planktic forams muddy packstone (MF-5), vi) Echinoderms and calcispheres pyritic wackestone/packstone (MF-6), and vii) Planktic forams wackestone/packstone (MF-7). Vertical distributions of the lithofacies and microfacies assemblages are presented in Fig. 4. Amongst the seven microfacies, MF-1, MF-2, MF-3 and MF-7 are associated with AL lithofacies (Fig. 4). The BL lithofacies consists of MF-1, MF-4, MF-5, and MF-6 (Fig. 4). Laminations are the primary sedimentary structures observed throughout the studied AR-F interval. Stylolites and minor fractures are commonly observed within all microfacies except MF-3 and MF-5 (Fig. 4).

4.1.1. MF-1: muddy allochem limestone

This microfacies is dominated by abundant planktic forams (Pl) (~14–34.5%), 6.5–20.5% of hollow spherical and elliptical calcispheres (blue arrow in Fig. 5), few quantities of thin-shelled pelagic bivalves (green arrows in Fig. 5) (0–6.5%), minor echinoderms (0–8%) and rare amounts of pelecypods (Pe) (0–2%). Occasionally, ostracods (0–1.5%) are observed within the micrite matrix (Mi) (Fig. 5). Minor amounts of calcite (C) and ferroan calcite (fC) filling bioclastic tests (Fig. 5a and d) along with rare amounts of black pyrite crystals (yellow arrow) are observed (Fig. 5c–d, g-h). The visual porosity is negligible. Thin sections reveal fracture porosity due to the shattering of grains (orange arrow) with very poor pore interconnectivity (Fig. 5a and b).

Interpretation: This microfacies refers to standard microfacies (SMF3): pelagic lime mudstone and wackestone with planktonic microfossils. The typical depositional environment is FZ 1: pelagic deep water basinal facies according to Flügel (2010). The dominant planktic forams characterize calm conditions and low-energy waves (Flügel, 1982, 2010). Accordingly, an open marine basinal depositional environment (between 100 m and 300 m) can be assigned to the microfacies (Gibson, 1989; Flügel, 2010).

4.1.2. MF-2: calcispheres and planktic forams wackestone/packstone

This microfacies consists of common amounts of planktic forams (Pl) (20–26.5%) and hollow spherical and elliptical calcispheres (blue arrows) (15.5–19%), rare amounts of ostracods (1–1.5%), pelecypods (0.5–1%), thin-shelled bivalves (green arrows) (0–1.5%) and echinoderms (E) (1–2%) along with abundant micrite matrix (Mi) (Fig. 6a and b). Ferroan calcite (fC) is observed (2–6.5%) filling bioclastic tests (Fig. 6b) along with rare amounts of calcite, ferroan dolomite, dolomite and pyrite crystals. The MF-2 has negligible visual porosity; however, fracture porosity (orange arrow) was observed (Fig. 6b).

Interpretation: Planktonic foraminifers usually indicate calm conditions and low-energy waves (Flügel, 1982). The filaments may be derived from pelecypods which are planktic gastropods, or from very thin-shelled bivalves which are typically found in open marine environments. The continuity of planktonic foraminifera appearance and the absence of benthic foraminifera in the MF-2 facies indicate deep marine basinal settings (Flügel, 2013).

4.1.3. MF-3: calcispheres wackestone/packstone

The MF-3 microfacies comprise common amounts of hollow spherical and elliptical calcispheres (blue arrows) (~27.5%), minor amounts of planktic forams (Pl) (~6%), pelecypods 'Ostrea' (Pe) and rare amounts of echinoderms and ostracods (Fig. 6a and b). The MF-3 has

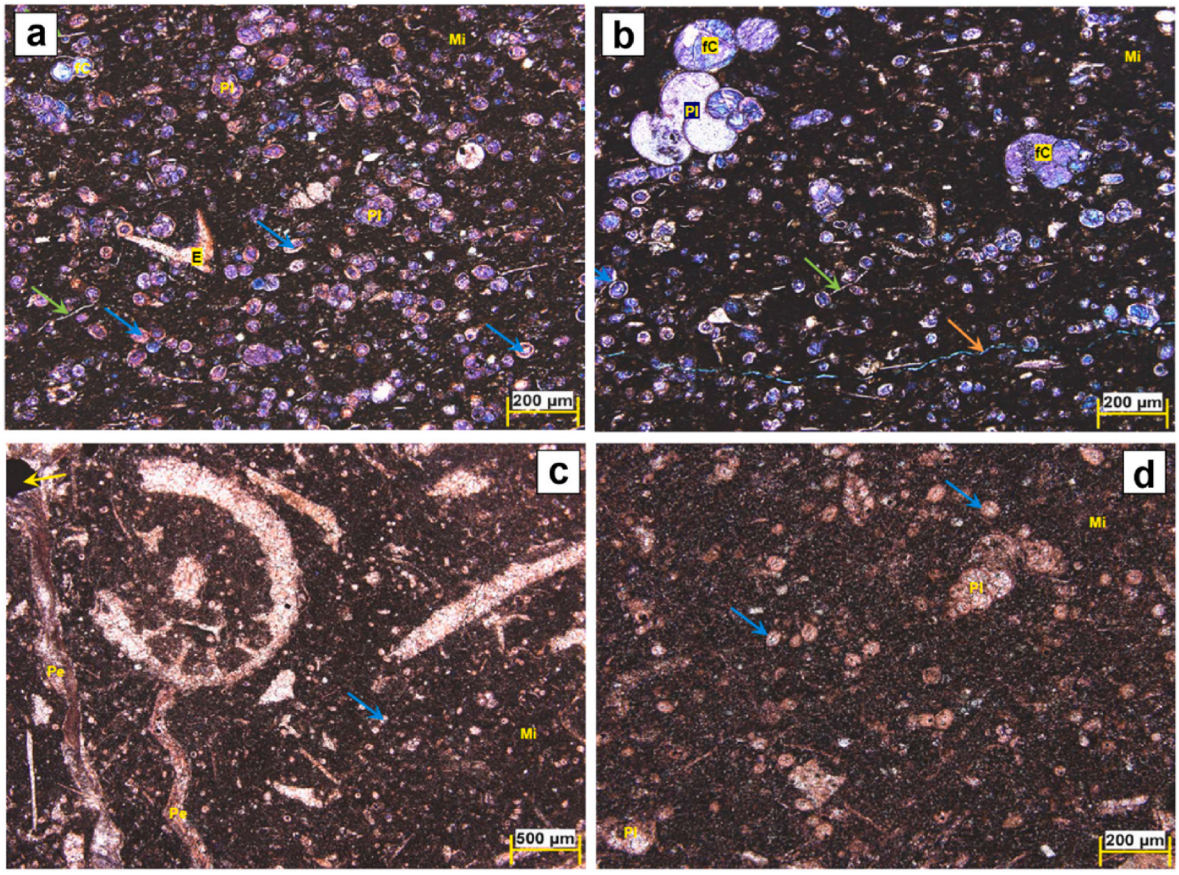

Fig. 6. Thin section photographs of the microfacies MF-2 under plane-polarized light (PPL) at (a) 10378.01 ft and (b) 10379.04 ft, indicating the presence of micritic matrix (Mi), frequent planktic forams (Pl), calcispheres (blue arrows), rare amounts of ostracods, pelecypods, pelagic bivalves (green arrows) and echinoderms (E), ferroan calcite (fC). Orange arrow indicates fracture porosity; (c–d) MF-3 under PPL at 10384.03 ft, exhibiting micrite matrix with common quantities of calcispheres, minor planktic forams, pelecypods 'Ostrea' (Pe), and pyrite crystal (yellow arrow). (For interpretation of the references to colour in this figure legend, the reader is referred to the Web version of this article.)

about 50% micrite matrix with rare amounts of calcite and black pyrite crystals.

Interpretation: Matrix dominance and abundant calcispheres with planktic forams indicate open marine calm conditions. During the Cretaceous, oysters typically inhabited shallow-water environments of the Tethys near North Africa (Dhondt et al., 1999; Bauer et al., 2003). But these became scarce at times of high sea-levels during Late Cenomanian-Early Turonian (Dhondt et al., 1999; Gertsch et al., 2010; Ahmad et al., 2015). In the MF-3 microfacies, we observed very minor amounts of Ostrea; and we can link the scarcity of such pelecypods to high sea-level conditions during the AR-F deposition.

4.1.4. MF-4: calcispheres, pelagic bivalves and planktic forams packstone

It mostly consists of planktic forams (Pl) (19–21%), hollow spherical and elliptical calcispheres (blue arrows) (~15%) and thin-shelled bivalves (green arrows) (10–12%) as the major skeletal grains along with rare amounts of pelecypods (Pe), echinoderms (E) and ostracods (Fig. 7a). Micrite forms the matrix which has an abundance of around 40–42%. Minor amounts of calcite (C), rare amounts of ferroan calcite (fC; filling bioclastic tests), black pyrite crystals and traces of dolomite (D) are also identified (Fig. 7a).

Interpretation: Dominance of planktic forams in this packstone microfacies points to a calm marine depositional environment (e.g., Berggren and Miller, 1989; Flügel, 2013). The filaments are derived from pelecypods, or from very thin-shelled bivalves, which are typically found in deeper marine environments.

4.1.5. MF-5: echinoderms, calcispheres and planktic forams muddy packstone

MF-5 microfacies is made up of common amounts of planktic forams (Pl) (~16%), hollow spherical and elliptical calcispheres (blue arrows) (18%) and echinoderms (E) (20%) as the principal skeletal grains within micrite matrix (Fig. 7b). The minor amount of pelecypods (Pe) is also present together with the ferroan calcite (fC) as a filling material for the bioclastic tests.

Interpretation: Based on the presence of planktic forams, absence of benthic forams, and high percentages of marine echinoderms, we infer low energy, calm open marine deeper water depositional condition for this microfacies.

4.1.6. MF-6: echinoderms and calcispheres pyritic wackestone/packstone

The skeletal grains of the MF-6 comprise the hollow spherical and elliptical calcispheres (blue arrows) (~25%) and echinoderms (E) (~20%) along with minor planktic forams (Pl) (5–6%) (Fig. 7c). Micrite matrix has an abundance of 30% by volume. Black pyrite crystals (yellow arrows) are very commonly observed (Fig. 7c), around 11% by volume, along with minor amounts of ferroan calcite filling the tests.

Interpretation: Dominant constituents, i.e., echinoderms along with minor planktic forams indicate calm energy and open marine conditions for deposition. Benthic forams are absent. The common presence of pyrites indicates a reducing condition was prevalent, which can be expected in a deeper marine environment.

4.1.7. MF-7: planktic forams wackestone/packstone

The principal skeletal grain of the MF-7 is planktic forams (Pl)

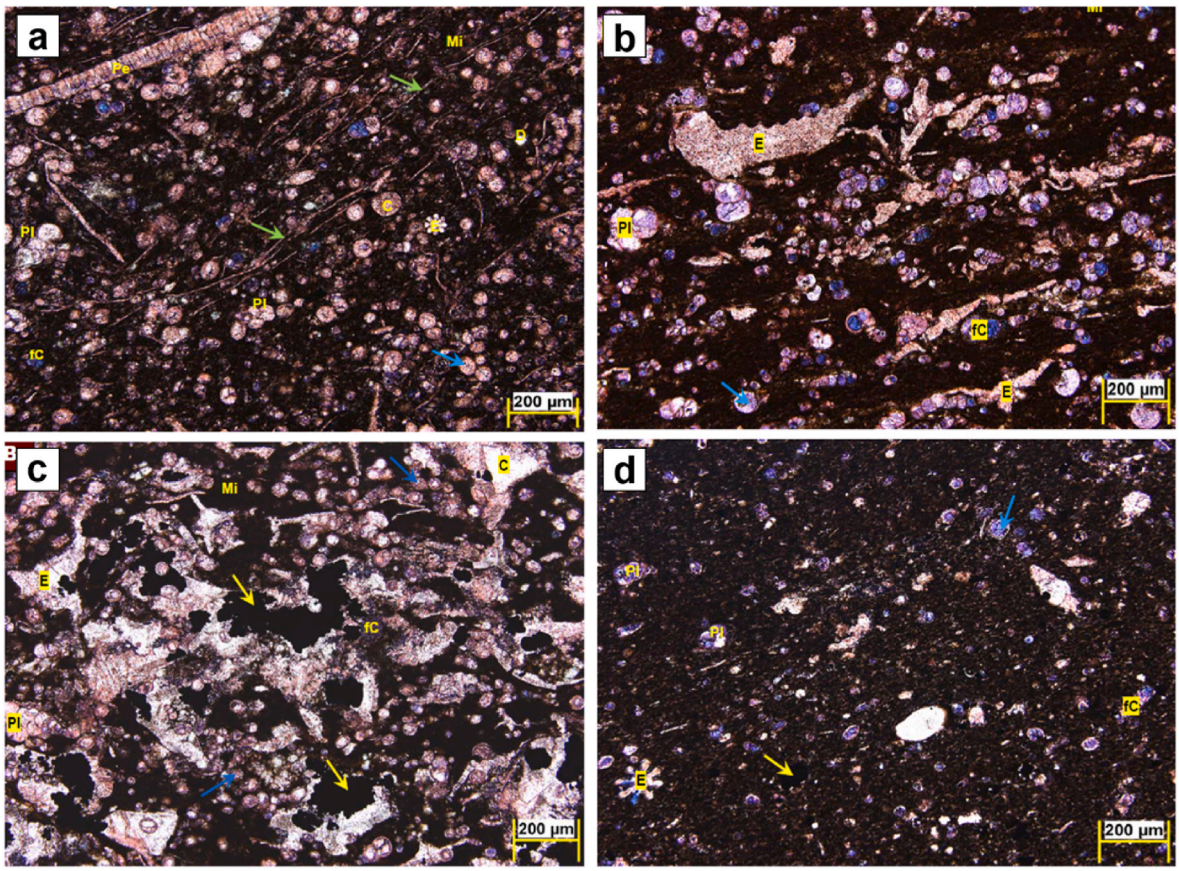

Fig. 7. Thin section photographs of the microfacies (a) MF-4 at 10419.03 ft, (b) MF-5 at 10457.03, (c) MF-6 at 10457.03 ft; and (d) MF-7 at 10474.08 ft, indicating the presence of micritic matrix (Mi), echinoderms (E), with frequent to minor amounts of planktic forams (Pl), calcispheres (blue arrows), pelagic bivalves (green arrows) and minor amounts of pelecypods (Pe). (For interpretation of the references to colour in this figure legend, the reader is referred to the Web version of this article.)

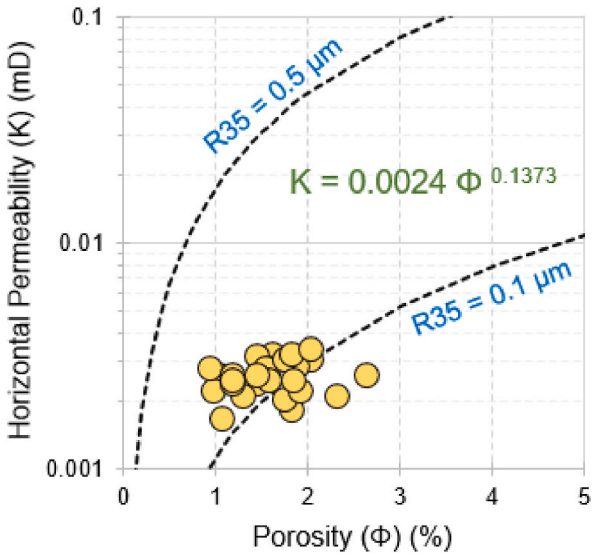

Fig. 8. Relationships between core-measured (a) porosity (Φ) and horizontal permeability (K) in the AR-F Member.

(21.5–32% by volume) (Fig. 8c–f). Minor quantities of calcispheres (5.5–8%) and echinoderms (E) (2.5–8.5%) are also observed. Micrite matrix has an abundance of 35.5–49.5% by volume. Minor amounts of ferroan calcite (fC) (6–6.5%) are seen filling the bioclastic tests. Rare amounts of black pyrite crystals (yellow arrows) are also observed (1–1.5% by volume) (Fig. 7d).

Interpretation: In this microfacies, the planktic forams are still dominant, which points towards low energy depositional environment, i.e., deep marine conditions (e.g., Gibson, 1989; Berggren and Miller, 1989; Flügel, 2013).

4.2. Diagenetic features in the AR-F

The detailed petrographic analysis exhibits several diagenetic processes: i) micritization, ii) calcite cementation, iii) minor dolomitization (as indicated by the presence of dolomite within the matrix), iv) pyritization, v) minor dissolution, vi) mechanical compaction and vii) chemical compaction. All the studied samples are dominated by micrite matrix, between 31 and 50.5% by volume, indicating micritization to be the most dominant diagenetic agent. Cementation is identified as the second most dominant process. Calcite is the dominating cement. These cements mostly occur as filling bioclast tests/chambers and fractures with some amounts are observed scattered throughout the matrix. Pyrites were probably formed at the later stages of the diagenesis. The minor presence of vuggy pores in CT scan images indicates non-fabric selective dissolution. The presence of minor fracturing indicates some degree of mechanical compaction. We observed minor rectangular or columnar stylolites within the AR-F which indicates chemical compaction in the last stage of diagenesis as a result of overburden pressure or tectonic stress.

4.3. Petrophysical properties

The routine core analysis (RCAL) indicates that the AR-F Member is

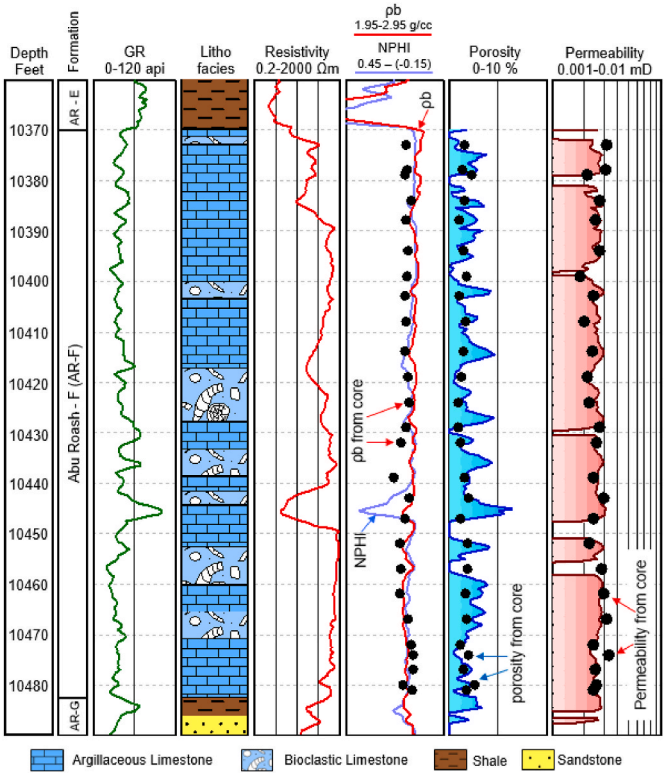

Fig. 9. Vertical distribution of the lithofacies and petrophysical properties within the AR-F Member. Black dots indicate the core measurements. GR, ρb, and NPHI denote gamma-ray, bulk-density, and neutron porosity, respectively.

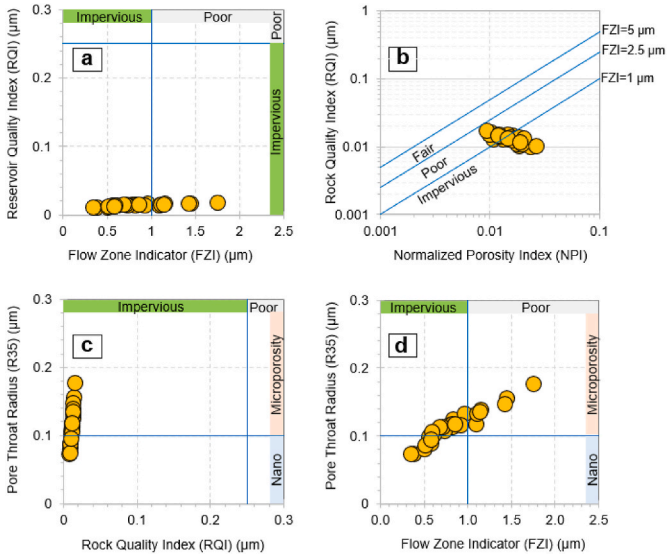

Fig. 10. Reservoir characterization by plotting the relationship of RQI with (a) FZI and (b) NPI; Estimated Pore throat radius (R35) is plotted with (c) RQI and (d) FZI for both the lithofacies types interpreted in the AR-F Member, data belongs to the Well AG-121. RQI, FZI, and NPI calculations are based on Amaefule et al. (1993). R35 is based on Winland (1972).

very tight with 0.9–2.6% porosity (Fig. 8). The horizontal permeability varies between 0.0016 and 0.0033 mD and the inferred Φ-K relationship is as below (Fig. 8):

$$K = 0.0024\Phi^{0.1373} \quad (1a)$$

Vertical distribution of porosity and permeabilities across the cored interval along with the wireline log responses of the AR-F Formation from the well AG-121 is presented in Fig. 9. AR-F exhibits low gamma ray (30–60 api), high resistivity (>250 Ωm), 2.64–2.74 g/cc bulk-density (Fig. 9) The quality of the AR-F Formation has been characterized by RQI, NPI, and FZI parameters. The formation is characterized by low RQI values (<0.01 μm) which is indicative of very poor reservoir quality (i.e., impervious) (Fig. 10). Due to the very poor permeabilities, the studied samples exhibit FZI <1 μm (Fig. 10a and b) confirming the impervious nature while seven measurements indicate FZI >1 μm with maximum FZI reaching up to 1.76 μm. This represents the poor-quality zones (1 μm < FZI <2.5 μm), indicating the possible influence of the minor fractures within the AR-F. We investigated the CT scan images of the core plugs and observed that the AR-F limestone is generally massive in nature. However, it revealed thin hairline fractures (Fig. 11a–c) and minor vuggy or fracture pores (Fig. 11d and e) which can locally improve the reservoir quality. These secondary pores are isolated, and the lack of connectivity will not considerably increase the permeability and hence the effective natural flow potential of the massive limestone lithofacies might be very poor. We also observed some traces of pyrite nodule in the CT scan (Fig. 11f). Since the MICP data were unavailable, we estimated pore throat sizes from core-based porosity-permeability properties. The AR-F consists of nano- and microporosities with R35 ranging between 0.07 and 0.18 μm (Fig. 10). The SEM images also reveal isolated nanopores confirming the tight behavior (Fig. 12). A summary of the core-based petrophysical properties of the AR-F Member is presented in Table 1.

4.4. Geochemical properties

4.4.1. Source rock characteristics

The quantity of organic matter contained in a rock is generally estimated as TOC and represented as a weight percentage. The measured TOC values of the analyzed AR-F samples vary between 0.59 and 3.57 wt % (Fig. 13) with an average TOC of 2.2 wt%. The majority of the data suggests TOC >1.5 wt%. The MF-1 microfacies has the highest TOC content when compared to the other microfacies intervals. The Rock-Eval pyrolysis T_{max} values of the 22 samples range from 435 to 441 °C and have an average value of 438.5 °C (Fig. 13), which signifies that the AR-F is thermally matured and falls within the oil generation window.

The S_1 and S_3 values of the AR-F range between 0.78 and 5.45 mgHC/gRock and 0.11–0.37 mgHC/gRock, respectively (Fig. 13). The S_2 yields the generative potential of a source rock, and this is a more reliable measure of source rock potential. The S_2 values of the studied AR-F carbonate sample range between 1.84 and 19.9 mgHC/gRock with a majority of the values indicating >6 mgHC/gRock (Fig. 13), which indicates a very good to excellent source rock potential (Peters and Cassa, 1994; Peters, 2018). Based on the Rock-Eval Pyrolysis results, the Oxygen Index (OI) varies between 4 and 30 $mgCO_2$/gTOC. Production Index (PI) varies between 0.05 and 0.52.

A cross plot between pyrolysis T_{max} and PI (Fig. 14a) indicates few data points with PI < 0.1 which infers that these samples are not capable of thermogenic hydrocarbon generation, despite T_{max} being more than 435 °C (Peters and Cassa, 1994). However, the majority of the data points indicate PI > 0.1 are believed to have generated hydrocarbons or maybe generating at present (Fig. 14a). Hydrogen Index (HI) is observed to be 311–570 mgHC/gTOC, while the data distribution reveals majority with HI > 400 mgHC/gTOC. Fig. 14b depicts the HI against pyrolysis T_{max}, which reveals matured Type-II organic matter within the oil window. The measured GP is in the range of 3.83–22.71 mgHC/gRock indicating good to very good generative potential (Fig. 15a). A cross plot between Rock-Eval S_1–S_2 indicates indigenous hydrocarbons present within the samples (Fig. 15b). Measured TOC and S_2 exhibit a good to very good source rock potential within the AR-F Member (Fig. 16a). TOC vs S_1 cross plot (Fig. 16b) indicates oil cross-over behavior in the majority of the samples. High oil cross-over is indicative of high free oil content and active hydrocarbon generation and expulsion (Jarvie,

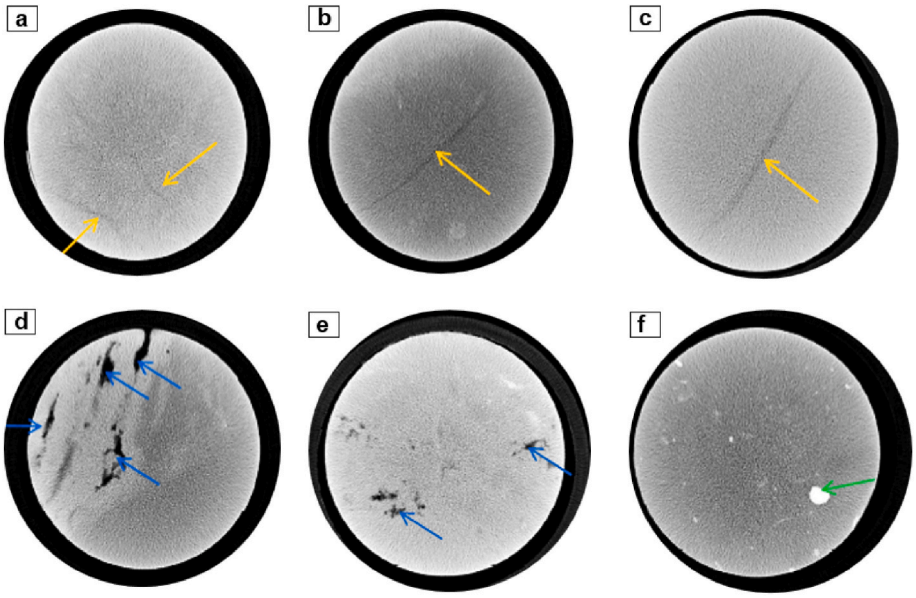

Fig. 11. CT scan images of the core plugs from the AR-F Member, Well AG-121. The orange arrows mark natural hair-line fractures at (a) 10,382 ft, (b) 10,376 ft, and (c) 10,444 ft; blue arrows mark vuggy/fracture pores at (d) 10,421 ft, and (e) 10,441 ft; (f) green arrow indicates pyrite nodule at 10,477 ft. (For interpretation of the references to colour in this figure legend, the reader is referred to the Web version of this article.)

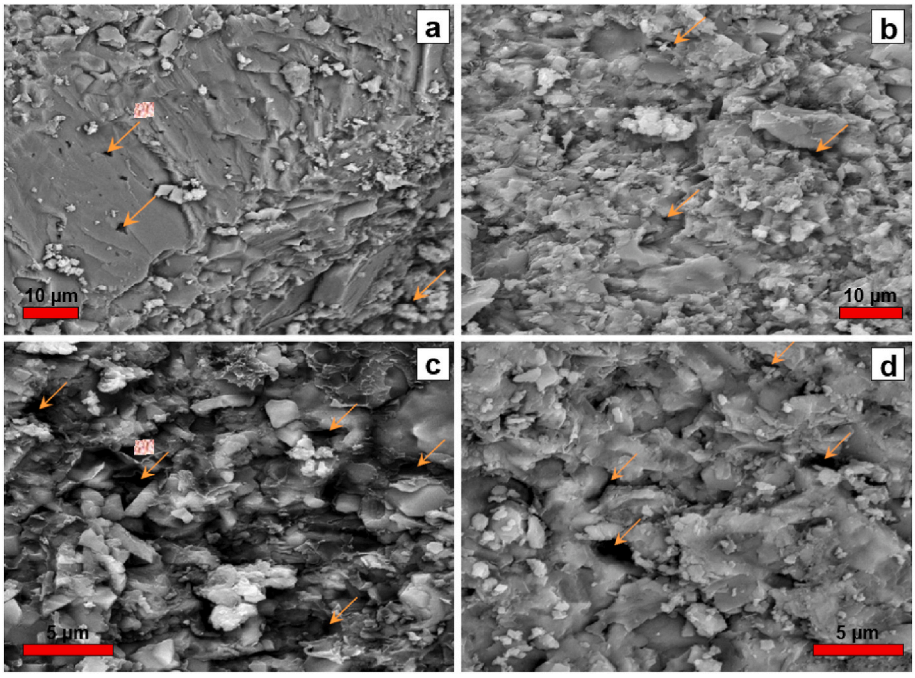

Fig. 12. SEM images of the AR-F Member, Well AG-121 at (a) 10384.03 ft (MF-3), (b) 10419.03 ft (MF-4), (c) 10462.01 ft (MF-1); and (d) 10,472 ft (MF-2), respectively. Orange arrows indicate pore spaces. (For interpretation of the references to colour in this figure legend, the reader is referred to the Web version of this article.)

2012). The oil cross-over effect is a simple means to identify potential reservoir intervals with potentially producible oils indicated by high oil cross-over.

4.4.2. XRF analysis

We analyzed the X-Ray Fluorescence data to investigate the elemental chemistry of the studied AR-F carbonate formation. Results are presented in Fig. 17. The elemental concentrations indicate that Calcium (Ca) is the most abundant element ranging between 33 and 51 wt% (mostly >40 wt%). Silicon (Si) varies between 0.76 and 28 wt%, although it is mostly <5 wt%. We observed a consistently low Si/Ca ratio (<0.2) which indicates that the clastic influx had been minimal (Olde et al., 2015). Apart from Si, we also utilized Aluminum (Al) and Titanium (Ti) as a proxy for detrital influx (Jarvis et al., 2001). We observed Al and Ti concentrations varying between 2866-100340 ppm and 227–8062 ppm, respectively, which provided a range of Ti/Al ratio between 0.02 and 0.11 within the AR-F Member. However, Ti/Al ratio has mostly been below 0.05 and this poor value also indicates minimal detrital influx and dilution effect. We observed an increasing Ti/Al trend within MF-7 at the lowermost part of the AR-F where Ti/Al ratio

Table 1
Summary of the petrophysical properties of the AR-F Member based on the core measurements. 'Avg', 'SD' and 'CV' refer to the average values, standard deviation and coefficient of variation, respectively.

Petrophysical characteristics	AR-F Formation				
	Min	Max	Avg	SD	CV
Porosity (Φ) (%)	0.949	2.656	1.613	0.421	0.261
Horizontal Permeability (Kh) (mD)	0.0017	0.0033	0.0025	0.0004	0.1725
Grain Density (gm/cc)	2.490	2.704	2.616	0.050	0.019
Bulk Density (gm/cc)	2.450	2.651	2.574	0.048	0.019
Mean Hydraulic Radius (mD)	0.300	0.538	0.405	0.057	0.141
Rock Quality Index (RQI) (μm)	0.0094	0.0169	0.0127	0.0018	0.1412
Normalized Porosity Index (NPI)	0.010	0.027	0.016	0.004	0.266
Flow Zone Indicator (FZI) (μm)	0.3584	1.7631	0.8547	0.3428	0.4010
Pore Throat Radius (R35) (μm)	0.071	0.176	0.113	0.025	0.220

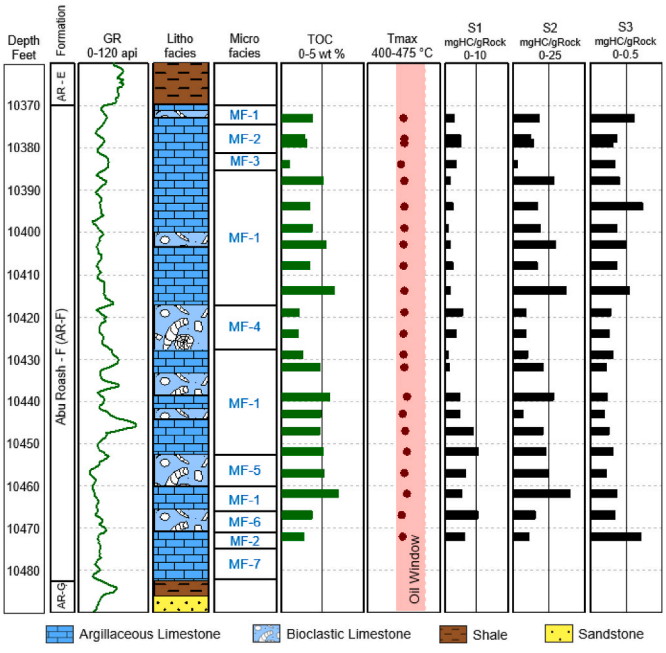

Fig. 13. Organic geochemical log of the AR-F Member in Well AG-121.

increases from 0.026 at 10,470 ft to 0.111 at the base of AR-F (10,482 ft). Molybdenum (Mo) and Vanadium (V) concentrations were used as anoxia proxy elements. Mo and V enrichments are indicative of redox conditions (Sageman et al., 2003). V concentration ranges between 55 and 569 ppm and was identified throughout the studied interval while Mo was only recorded between 10,438-10468 feet with a concentration range of 3–19 ppm. Manganese (Mn) accumulation typically signifies oscillating redox conditions (Calvert and Pedersen, 1996). Mn concentration varies between 123 and 835 ppm. It is usually low (<500 ppm) in most of the AR-F interval, which indicates that any Mn-bearing minerals are likely to be minor constituents of the reservoir. However, a higher Mn concentration (>400 ppm) is recorded in the lowermost AR-F (10,470-10482 ft), which may refer to the increasing oxic condition at the bottom of the AR-F (Jarvis et al., 2008). Ni and V enrichments are indicative of nutrient supply (Algeo and Maynard, 2004). Ni concentration varies between 51 and 115 ppm; however, it is very consistent around 65–76 ppm throughout the interval.

Based on the analysis the studied AR-F carbonate interval confirms overall poor clastic/detrital influx. The lower part of AR-F between 10,432-10469 feet is characterized by the lowest Si concentration (<3 wt%), lowest Ti/Al ratio, higher Mo (4–19 ppm) and consistently higher V concentration (120–441 ppm) indicating a highly anoxic depositional condition that maintained greatly reducing environment. The same interval also consists of the highest TOC (~2.5 wt%) which was favored by the anoxia. Right below this zone, we observed increasing trends in Ti/Al ratio, Si, and Mn concentrations as well as a decreasing trend in V concentration, which reflects the oxic condition in the bottom-most part of the AR-F Member, which falls in the depth range between 10,469-10482 feet.

5. Discussions

5.1. Depositional environment of AR-F

Depositional settings of AR-F are not much discussed in the literature. All the microfacies within AR-F, dominantly consisting of planktonic foraminifera in association with abundant calcispheres and absence of benthic forams, characterize calm conditions and low energy waves, indicating an open-marine, deep-water setting (Flügel, 2004). Thin shell fragments noted during core logging represent larval or juvenile shells of pelagic bivalves. Thin-shelled pelagic bivalves (filaments) are common constituents of Mesozoic deep marine basinal limestones. These, along with the lack of benthonic foraminifera are suggestive of a deeper water deposition, most likely bathypelagic. Core logging observations and thin section analysis reveal the presence of pyrites throughout the studied cores, which occur as an authigenic mineral. Macroscopically, small aggregates of pyrite crystals are locally noted in the various facies' types. Authigenic pyrite commonly forms under reducing conditions replacing organic material or in proximity to organic material (Flügel, 2004) which translates to a calm condition in deep water settings. Minor dolomitization is locally observed in the studied cores. Based on the interpreted facies types and assemblages, we infer an open marine, relatively deep-shelf/basinal setting for AR-F. These observations corroborate well with Alsharhan and Abd El-Gawad (2008) and El Beialy et al. (2010) which also indicated a deep marine depositional environment for AR-F.

The elemental analysis by XRF also reveals critical information regarding the depositional environment. Higher Ca content consistent with a lower Al concentration throughout the studied AR-F interval is indicative of long-term high sea level (Jarvis et al., 2001; Olde et al., 2015; Mansour et al., 2020). Overall poor Ti/Al ratio indicates minimal detrital influx in general. An increase in Si, Mn, and Al with decreasing Ca towards the bottom-most part of the AR-F (10,469-10482 feet) suggests a local regression phase which possibly brought more silty/clayey content (Jarvis et al., 2008; Mansour et al., 2020). This interval also contains low TOC indicating oxic conditions. Based on the Mo and V enrichments and the poorest Si and Ti/Al ratio, the lower AR-F (10,432-10469 feet) is inferred as the most anoxic interval which positively correlates with the higher TOC accumulation when compared with the upper AR-F interval. This high TOC lower AR-F interval can be correlated with the observations made by Zobaa et al. (2011) from the Razzak oilfield in the North-Western Desert, where an increase in TOC (>10 wt %, maximum value reaching ~24 wt%) and an abrupt positive $\delta^{13}C_{org}$ excursion (~2.01‰) within the basal part of the AR-F have been reported. This was linked to the Late Cenomanian/Early Turonian (C/T) oceanic anoxic event (OAE2). During OAE events, oceans experience intensified oxygen deficiency which creates extreme reducing environments favorable for organic matter-rich sediment accumulation (Jenkyns, 2010). We did not have the isotope data. However, the entire Western Desert experienced organic-rich sedimentation during the late Cenomanian/early Turonian anoxia associated with a major global sea-level rise which deposited organic-rich shales, marls, and limestones on the oxygen-deprived shelf/slope regions and deep-sea basins of Northern Africa during the OAE2 (Bonarelli event, ~93 Ma) (Herbin et al., 1986; Klemme and Ulmishek, 1991; Lüning et al., 2004; Zobaa

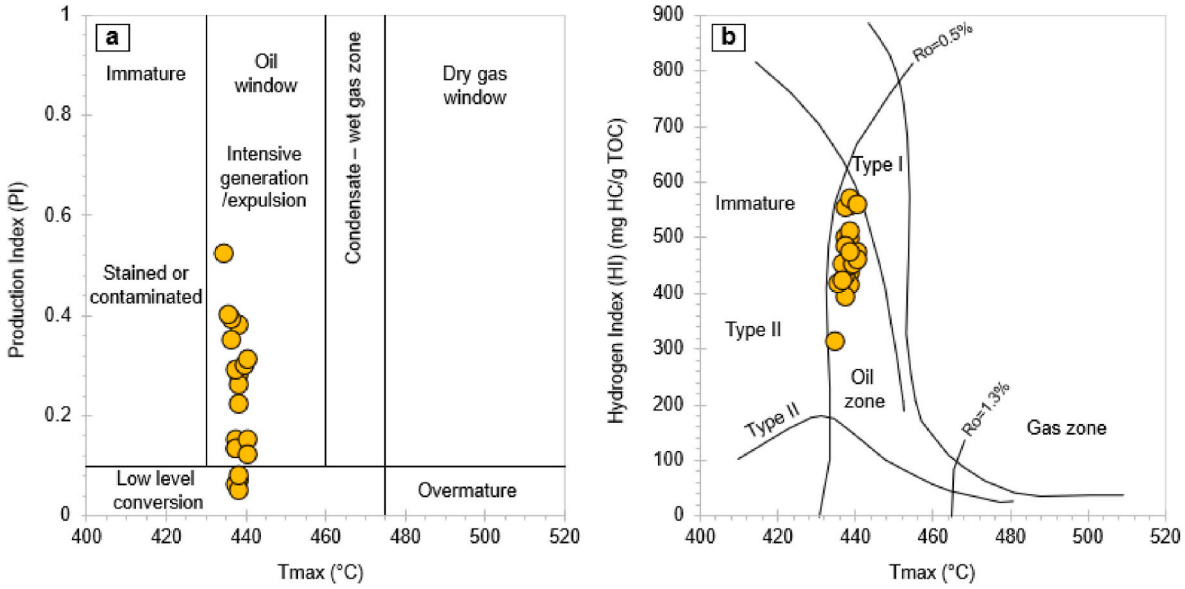

Fig. 14. (a) A cross plot between pyrolysis Tmax and PI indicates thermogenic hydrocarbon generation potential (after Peters, 1986), (b) A cross plot between pyrolysis Tmax and HI indicates maturity window and kerogen type of the AR-F carbonate samples (after Tyson, 1995).

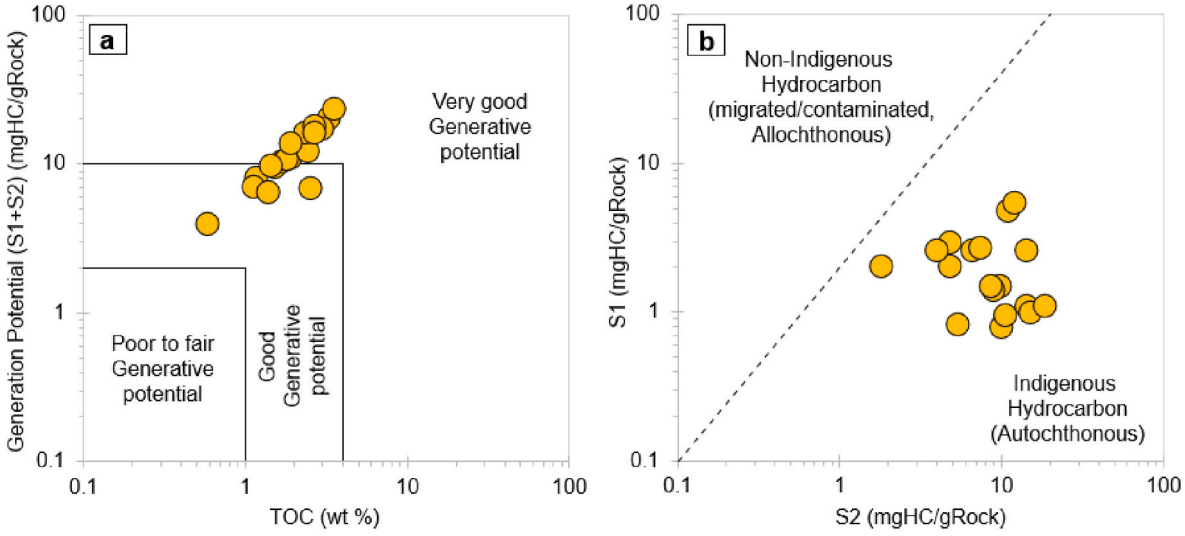

Fig. 15. (a) A cross plot between pyrolysis TOC and GP indicates good to very good hydrocarbon generation potential (after Maravelis and Zelilidis, 2010), (b) A cross plot between Rock-Eval S1–S2 indicates indigenous hydrocarbons (after Jarvie, 2012).

et al., 2009, 2011). Following the same, we can correlate the anoxic event in the 10,432-10469 feet interval of our studied AR-F Member in the well AG-121, which is well supported by Mo and V enrichment and coincides with the peak TOC measurement.

5.2. AR-F as a potential self-sourced reservoir

5.2.1. Source rock qualities of AR-F

Various researchers proposed different TOC limits to characterize carbonate source rock potential (Tissot and Welte, 1978, 1984; Hunt, 1979; Chen, 1985; Peters and Cassa, 1994; Qiu et al., 1998; Qin et al., 2004; Peng et al., 2008; Zhang et al., 2002; Huo et al., 2019) and indicate a range of 0.1–0.5 wt% threshold TOC value for an effective carbonate source rock. Due to weaker adsorption and retention capacities of carbonates than clays, Tissot and Welte (1984) took 0.3 wt% as a threshold TOC value in carbonate source rocks based on empirical observations. The AR-F Member has an average TOC of more than 1.5 wt%, with the highest TOC reaching 3.57 wt%. Based on the classification proposed by Peters (2018), the AR-F Member has fair to very good organic richness. Rock-Eval pyrolysis reveals that AR-F consists of Type-II organic matters that are thermally matured and fall within the oil generation window. High S_2 values, PI > 0.1 and fair to good generation potential make the AR-F carbonate a very good self-sourced interval with a high probability of oil production, as confirmed by the S_1-TOC relationship (Fig. 16b).

5.2.2. Reservoir quality of AR-F

Petrophysically the AR-F Member is homogenous but exhibits inferior qualities, characterized by < 3% porosity and <0.0033 mD horizontal permeability. The estimated RQI of <0.1 μm and FZI <2 μm are indicative of impervious to poor reservoir characteristics. AR-F is dominated by nano- and microporosities, as observed in the SEM images. We identified frequent thin fractures in the thin sections, and CT scan also revealed thin hairline fractures along with some minor vuggy

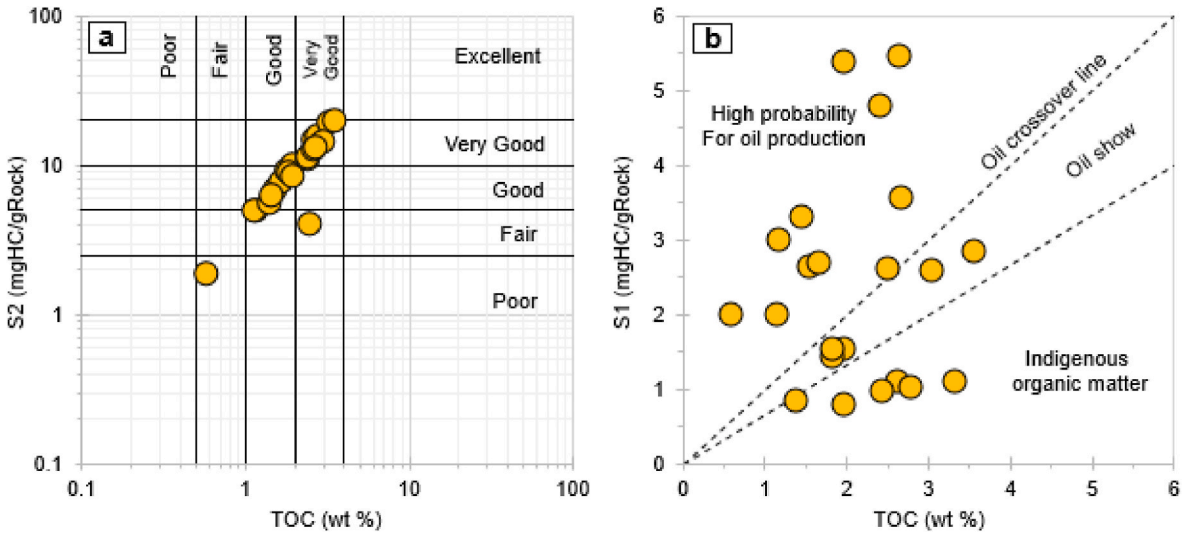

Fig. 16. (a) A cross plot between TOC and S2 indicates good to very good source rock potential of the AR-F carbonate samples (after Langford and Blanc-Valleron, 1990; Peters, 1986), (b) TOC-S1 cross plot illustrating the oil crossover effect of AR-F (after Jarvie, 2012).

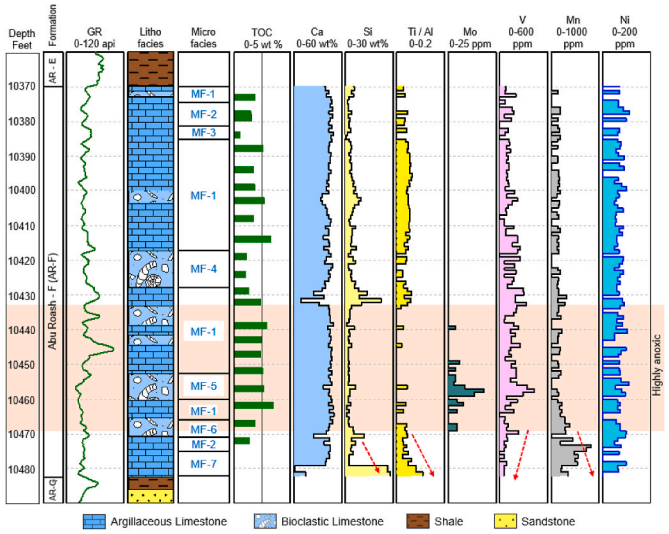

Fig. 17. Elemental profile of the AR-F Member based on the X-Ray Fluorescence data.

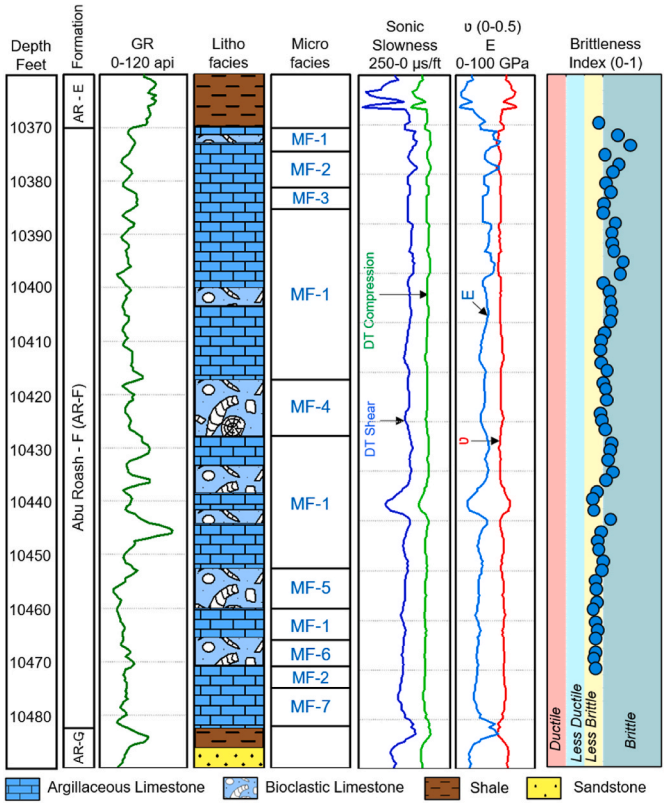

Fig. 18. Dynamic rock-elastic properties and brittleness index of the studied AR-F interval. The brittleness index is estimated following Grieser and Bray (2007). E = Young's modulus; υ = Poisson's ratio.

or fracture pores which may locally improve the reservoir quality. However, these secondary pores are isolated, and lack connectivity, which therefore, did not improve the flow capacity of AR-F. The gas chromatograph data from mud logging of the studied well indicated around 2000 ppm of methane (C1) and 300 ppm of ethane (C2) in the upper part of the AR-F between 10,370-10420 feet. The lower part of the AR-F (10,430-10470 feet) is associated with much higher C1 (10,000-40000 ppm) and C2 concentrations (1000–4000 ppm). This lower interval with higher gas content coincides with the high TOC (>2.5 wt%), anoxic zone of the AR-F (Fig. 13). Also, geochemical data of this interval plots within the oil show zone and beyond the oil cross-over line in the S_1-TOC cross plot (Fig. 16b) indicates a high probability of oil production. We conclude that this lower AR-F interval, despite being tight, is the most promising zone in terms of potentiality.

5.2.3. *Diagenetic controls on the petrophysical properties*

The detailed petrographic analysis of the carbonates from well AG-121 showed that the sedimentary succession of AR-F was affected by several diagenetic processes, which have either resulted in a significant decrease and minor increase in porosity and therefore diminished or improved the reservoir potentiality. Micritization is found to be the most dominant diagenetic process reducing the AR-F storage capacity. This is the first diagenetic phase, and it takes place in the marine diagenesis environment of limestone (Jafarian et al., 2018; Chafeet et al., 2020). This process usually fills up the pore throats and negatively impacts reservoir permeability. Micrite ranges between 31 and 50.5% by volume and acts as a reservoir quality destroying factor in AR-F. Pyrites were probably formed at the later stages of the diagenesis. We observed

rectangular or columnar stylolites within the AR-F, and based on the core-measured petrophysical properties, stylolites seem to be a reservoir quality destroying feature in AR-F. We observed minor fracturing indicating some degree of mechanical compaction. These may contribute to very minor porosity grain although fractures are mostly seen to be filled with calcite cements. The minor presence of vuggy pores in CT scan images indicates non-fabric selective dissolution. Connected vugs usually enhance reservoir permeability; however, the vugs within AR-F are mostly disconnected, therefore did not contribute to permeability enhancement.

5.2.4. Inferences on the unconventional reservoir development

To bring the carbonate reservoir into production, stimulation is absolutely necessary due to its tight nature. We analyzed the dynamic rock-elastic properties of the AR-F interval which exhibits ~0.28 Poisson's ratio (υ) and 23–47 GPa Young's modulus. We estimated the brittleness index using dynamic elastic properties following Grieser and Bray (2007), which yielded a range of 0.39–0.72 (Fig. 18). Results indicate that the upper part of the AR-F is brittle while the lower part is relatively less brittle. This interpretation is supported by the higher TOC content at the lower AR-F (Fig. 13) as well as higher Si and Ti/Al in the upper AR-F (Fig. 17). The overall brittle nature of the AR-F carbonate interval is indicative of good hydraulic fracturing success which is very necessary for bringing the tight interval into production.

The regional World Stress Map (WSM) database and Leila et al. (2021) indicated a N–S to NNE-SSW maximum horizontal stress orientation in the region, following which we infer that a horizontal well parallel to the E-W direction will be the most suitable choice which will facilitate geomechanically optimum hydraulic fracture propagation parallel to N–S, thus creating a transverse fracture network. Following the tight carbonate field development examples worldwide, especially in the Middle East and Egypt (Salamy et al., 2006; Al-Hajeri et al., 2007; George et al., 2012; Chimmalgi et al., 2013; Alyan et al., 2015; Sen et al., 2021), we recommend that coil tubing (CT) carried gun and acid stimulation will be helpful to activate this tight reservoir.

In March 2013, another well (AG-108) was drilled to test the argillaceous limestone reservoirs of AR-D Member which has <10 mD permeability. The well did not flow naturally and acid stimulation was conducted which showed oil and gas production rates of 2600 BOPD (barrel oil per day) and 6 MMSCFD (million standard cubic feet/day), respectively (EGPC, 2019). Horizontal well drilling through the AR-F with a slotted liner completion strategy is another effective way to ensure maximum reservoir contact (Salamy et al., 2008), as these perforated liners also provide increased accessibility for CT as well as acid jobs. It is to be noted that the optimum placement of horizontal wellbore should be guided by geomechanical understanding to ensure optimum mud weight and minimum wellbore instability. Latief et al. (2019) discussed the utility of an underbalanced drilling strategy to enhance production from carbonate reservoirs with poor permeability. The authors reported a threefold oil production increase as the bottomhole pressure was reduced by 20% below formation pressure during underbalanced drilling with nitrogen injection (Latief et al., 2019). A similar strategy has yet not been tested in any Egyptian carbonate reservoir but is worth considering.

6. Conclusions

This work presents a comprehensive petrographical, petrophysical, and preliminary geochemical characteristics of the Lower Turonian AR-F Member. The studied carbonates were deposited in a deep marine environment during lower Turonian, a period when a majority of the Northern African basins experienced oceanic anoxia associated with a global sea-level rise. The studied AR-F interval correlates to that phase of organic enrichments which yields a good to very good TOC content. The Type-II organic matters of the AR-F are thermally matured and fall within the oil generation window. The studied interval is very tight, and impervious with negligible permeabilities contributed by nano- and microporosities, which are far away from the conventional reservoir qualities. However, considering the self-sourcing abilities, AR-F Member can be considered as a potential unconventional reservoir that is usually observed to be tight worldwide. The mudlog gas data and geochemical analysis indicated a higher probability of oil production in the lower AR-F. We inferred that the porosity destroying diagenetic factors especially micritization have destroyed the storage capacity and reservoir development necessitates stimulation by hydraulic fracturing. It is to be noted that the present work only deciphered the AR-F characteristics from a single well due to limited core data availability. We recommend capturing more core data in future wells to decipher the lateral distribution and variation of AR-F properties across the Abu Gharadig field. However, this integrated study provided critical insights into the microfacies assemblage, depositional environment, and key petrophysical and geochemical properties of the AR-F Member. To confirm its production potential, AR-F Member should be perforated and tested with the recommended strategies. If successful, it can be quickly brought into completion and production strategy by combining it with already producing Abu Roash and Bahariya intervals using the same infrastructures, which can entirely change the economics of the field production.

Credit author statement

S. Farouk: Resources, Data curation, Project administration, Formal analysis, Writing -review & editing, Supervision. **S. Sen:** Conceptualization, Methodology, Resources, Formal analysis, Validation, Visualization, Software, Writing - original draft, Writing - review & editing. **S. S. Ganguli:** Resources, Validation, Writing - review & editing. **F. Ahmad:** Validation, Writing - review & editing. **M. Abioui:** Visualization, Resources, Validation, Writing - review & editing. **K. Al-Kahtany:** Resources, Validation, Writing - review & editing. **P. Gupta:** Resources, Formal analysis.

Declaration of competing interest

The authors declare that they have no known competing financial interests or personal relationships that could have appeared to influence the work reported in this paper.

Data availability

The authors do not have permission to share data.

Acknowledgments

The authors express their sincere gratitude to Prof. Massimo Zecchin (Editor-in-Chief) and Dr. Ahmed E. Radwan (Managing Guest Editor) for the excellent editorial handling. Critical and constructive comments by four anonymous reviewers are appreciated which benefited this work. The authors are grateful to Egyptian General Petroleum Corporation (EGPC) for the dataset and permission to publish this study. King Saud University (Riyadh, Saudi Arabia) supported the research project of K. Al-Kahtany (RSP-2021/139).

References

Abdel-Kireem, M.R., Schrank, E., Samir, A.M., Ibrahim, M.I.A., 1996. Cretaceous palaeoecology, palaeogeography and palaeoclimatology of the northern Western Desert, Egypt. J. Afr. Earth Sci. 22 (1), 93–112.

Abuamarah, B.A., Nabawy, B.S., 2021. A proposed classification for the reservoir quality assessment of hydrocarbon-bearing sandstone and carbonate reservoirs: a correlative study based on different assessment petrophysical procedures. J. Nat. Gas Sci. Eng. 88, 103807.

Adly, O., El Araby, A.M., El Barkooky, A., 2016. Abu Roash F member as a potential self-sourced reservoir in Abu Gharadig Basin, western Desert of Egypt. Santa Barbara,

California. In: AAPG Hedberg Conference, the Future of Basin and Petroleum Systems Modeling. April 3-8. Search and Discovery Article #90257.
Ahmad, F., Farouk, S., El-Kahtany, K., Al-Zubi, H., Diabat, A., 2015. Late cenomanian oysters from Egypt and Jordan. J. Afr. Earth Sci. 109, 283–295.
Algeo, T.J., Maynard, J.B., 2004. Trace-element behavior and redox facies in core shales of Upper Pennsylvanian Kansas-type cyclothems. Chem. Geol. 206 (3–4), 289–318.
Al-Hajeri, S.K., Ayoub, M.R., Al Shehhi, A.S., Negahban, S., Riberio, M.T., Bahamaish, J. N., 2007. Tight reservoirs – a development challenge example from a carbonate reservoir offshore Abu dhabi, uae. In: SPE Middle East Oil and Gas Show and Conference, Manama, Bahrain, March 11-14. SPE-105420-MS.
Alsharhan, A.S., Abd El-Gawad, E.A., 2008. Geochemical characterization of potential Jurassic/Cretaceous source rocks in the Shushan basin, northern Western Desert, Egypt. J. Petrol. Geol. 31 (2), 191–212.
Alyan, M., Martin, J., Irwin, D., 2015. Field development plan optimization for tight carbonate reservoirs. In: SPE Abu Dhabi International Petroleum Exhibition and Conference. UAE, Abu Dhabi. Nov 9-12. SPE-177695-MS.
Amaefule, J., Altunbay, M., Tiab, D., Kersey, D., Keelan, D., 1993. Enhanced reservoir description, using core and log data to identify hydraulic (flow) units and predict permeability in uncored intervals/wells. Houston, Texas. In: SPE Annual Technical Conference and Exhibition. SPE-26436-MS.
Awad, M.G., 1984. Habitat of oil in Abu Gharadig and faiyum basins, western Desert, Egypt. AAPG Bull. 68 (5), 564–573.
Bauer, J., Kuss, J., Steuber, T., 2003. Sequence architecture and carbonate platform configuration (late cenomanian–santonian), sinai, Egypt. Sedimentology 50 (3), 387–414.
Bayoumi, A.I., Lotfy, H.I., 1989. Modes of structural evolution of Abu Gharadig Basin, western Desert of Egypt as deduced from seismic data. J. Afr. Earth Sci. 9 (2), 273–289.
Berggren, W.A., Miller, K.G., 1989. Cenozoic bathyal and abyssal calcareous benthic foraminiferal zonation. Micropaleontology 35 (Suppl. 4), 308–320.
Bosworth, W., El-Hawat, A.S., Helgeson, D.E., Burke, K., 2008. Cyrenaican "shock absorber" and associated inversion strain shadow in the collision zone of northeast Africa. Geology 36 (9), 695–698.
Boutaleb, K., Baouche, R., Sadaoui, M., Radwan, A.E., 2021. Sedimentological, petrophysical, and geochemical controls on deep marine unconventional tight limestone and dolostone reservoir: insights from the Cenomanian/Turonian oceanic anoxic event 2 organic-rich sediments, Southeast Constantine Basin, Algeria. Sediment. Geol. 429, 106072.
Bryndzia, L.T., Braunsdorf, N.R., 2014. From source rock to reservoir: the evolution of self-sourced unconventional reservoir plays. Elements 10 (4), 271–276.
Calvert, S.E., Pedersen, T.F., 1996. Sedimentary geochemistry of manganese: implications for the environment of formation of manganiferous black shales. Econ. Geol. 91 (1), 36–47.
Chafeet, H.A., Raheem, M.K., Dahham, N.A., 2020. Diagenesis processes impact on the carbonate Mishrif quality in Ratawi oilfield, southern Iraq. Model. Earth Syst. Environ. 6 (4), 2609–2622.
Chen, J.Q., Pang, X.Q., Wu, S., Chen, Z.H., Hu, M.L., Ma, K.Y., Pang, B., Hua, Z.P., 2020. Method for identifying effective carbonate source rocks: a case study from Middle-Upper Ordovician in Tarim Basin, China. Petrol. Sci. 17 (6), 1491–1511.
Chen, P.J., 1985. Comment on several topics in the geochemistry carbonate source rock. Pet Geol. Exp. 7 (1), 3–12.
Chimmalgi, V.S., Al-Humond, J., Al-Sabea, S., Gazi, N., Bardalaye, J., Mudavakkat, A., Al-Enezi, H., Al-Zankawi, O., Ahsan, J., Abdulrazzaq, E., Tirkey, N., Kotecha, R., Snasiri, F., Jalan, S., Al-Zabbi, R., Al-Dousari, M., Al-Othman, M., Al-houti, N., Benamer, N., Elsherif, T., Surjaatmadja, J., Elmofti, M., 2013. Reactivating a tight carbonate reservoir in the greater burgan field: challenges, options and solutions. In: SPE Middle East Oil and Gas Show and Conference. Manama, Bahrain. March 10-13. SPE-164248-MS.
Dhondt, A.V., Malchus, N., Boumaza, L., Jaillard, E., 1999. Cretaceous oysters from North Africa: origin and distribution. Bull. Soc. Geol. Fr. 170 (1), 67–76.
Dunham, R.J., 1962. Classification of carbonate rocks according to depositional texture in Classification of Carbonate Rocks. AAPG Mem 1, 108–121.
Egyptian General Petroleum Corporation (EGPC) 2019 Production: Whole Drilling Report 2p.
El Atfy, H., 2011. Cretaceous Palynology of the GPTSW-7 Well, Western Desert, Egypt. LAP LAMBERT Academic Publishing, Saarbrücken.
El Beialy, S.Y., El Atfy, H.S., Zavada, M.S., El Khoriby, E.M., Abu-Zied, R.H., 2010. Palynological, palynofacies, paleoenvironmental and organic geochemical studies on the Upper Cretaceous succession of the GPTSW-7 well, north Western Desert, Egypt. Mar. Petrol. Geol. 27 (2), 370–385.
El Diasty, W., 2014. Khatatba formation as an active source rock for hydrocarbons in the northeast Abu Gharadig Basin, north western Desert, Egypt. Arabian J. Geosci. 8 (4), 1903–1920.
El Gazzar, A.M., Moustafa, A.R., Bentham, P., 2016. Structural evolution of the Abu Gharadig field area, northern western Desert, Egypt. J. Afr. Earth Sci. 124, 340–354.
El-Sherbiny, H.M., 2002. Petrophysical Evaluation of Abu El-Gharadig Basin, Egypt. Ph. D. Dissertation,. Cairo University.
Farouk, S., Sen, S., Abuseda, H., El-Shamly, Y., Salam, A., Elhossainy, M.M., 2022. Petrophysical characterization of the turonian and cenomanian intervals in the Abu Gharadig field, western Desert, Egypt: inferences on reservoir quality and resource development. Nat. Resour. Res. 31 (3), 1793–1824. https://doi.org/10.1007/s11053-022-10069-0.
Farouk, S., Sen, S., Ganguli, S.S., Abuseda, H., Debnath, A., 2021. Petrophysical assessment and permeability modelling utilizing core data and machine learning approaches – a study from the Badr El Din-1 field, Egypt. Mar. Petrol. Geol. 133, 105265.
Flügel, E., 2013. Microfacies of Carbonate Rocks: Analysis, Interpretation and Application, third ed. Springer Science and Business Media, Berlin/Heidelberg.
Flügel, E., 2010. Microfacies of Carbonate Rocks: Analysis, Interpretation and Application, second ed. Springer-Verlag, Berlin Heidelberg, New York.
Flügel, E., 2004. Microfacies of Carbonate Rocks: Analysis, Interpretation and Application, first ed. Springer, Heidelberg.
Flügel, E., 1982. Microfacies Analysis of Limestones. Springer, Berlin.
Ganguli, S.S., Sen, S., Verma, S., 2021. Characterization of organic content, brittleness index and geomechanical properties of the Eocene Cambay Shales – insights from the Ankleshwar oil field in Western India. Interpretation 9 (1), T235–T252.
George, B.K., Clara, C., Al Mazrooei, S., Manseur, S., Abdou, M., Chong, T.S., Al Raeesi, M., 2012. Challenges and key learning for developing tight carbonate reservoirs. In: Abu Dhabi International Petroleum Exhibition and Conference (ADIPEC), Abu Dhabi. UAE. Nov 11-14. SPE-161693-MS.
Ghassal, B.I., Littke, R., Atfy, H.E., Sindern, S., Scholtysik, G., 2018. Source rock potential and depositional environment of Upper Cretaceous sedimentary rocks, Abu Gharadig Basin, Western Desert, Egypt: an integrated palynological, organic and inorganic geochemical study. Int. J. Coal Geol. 186, 14–40.
Gibson, T.G., 1989. Planktonic benthonic foraminiferal ratios: modern patterns and Tertiary applicability. Mar. Micropaleontol. 15 (1–2), 29–52.
Gertsch, B., Keller, G., Adatte, T., Berner, Z., Kassab, A.S., Tantawy, A.A.A., El-Sabbagh, A.M., Stueben, D., 2010. Cenomanian–Turonian transition in a shallow water sequence of the Sinai, Egypt. Int. J. Earth Sci. 99 (1), 165–182.
Grieser, W.V., Bray, J.M., 2007. Identification of production potential in unconventional reservoirs. In: Production and Operations Symposium. Oklahoma City, Oklahoma, USA. SPE-106623-MS.
Guiraud, R., Maurin, J.C., 1992. Early cretaceous rifts of western and central Africa: an overview. Tectonophysics 213 (1–2), 153–168.
Hantar, G., 1990. North western Desert. In: Said, R. (Ed.), The Geology of Egypt. A.A. Balkema, Rotterdam, Brookfield, pp. 293–319.
Herbin, J.P., Montadert, L., Muller, C., Gomez, R., Thurow, J., Wiedmann, J., 1986. Organic-rich sedimentation at the cenomanian-turonian boundary in oceanic and coastal basins in the north atlantic and Tethys. Geol. Soc. London, Spec. Publ. 21 (1), 389–422.
Hewaidy, A.G., Elshahat, O.R., Kamal, S., 2018. Stratigraphy, facies analysis and depositional environments of the upper unit of Abu Roash "E" member in the Abu Gharadig field, western Desert, Egypt. J. Afr. Earth Sci. 139, 26–37.
Hunt, J.M., 1979. Petroleum Geochemistry and Geology. W.H. Freeman and Company, New York.
Huo, Z.P., Pang, X.Q., Chen, J.Q., Zhang, J., Song, M., Guo, K., Li, P., Li, W., Liang, Y., 2019. Carbonate source rock with low total organic carbon content and high maturity as effective source rock in China: a review. J. Asian Earth Sci. 176, 8–26.
Jafarian, A., Javanbakht, M., Koeshidayatullah, A., Pimentel, N., Salad Hersi, O., Yahyaei, A., Beigi, M., 2018. Paleoenvironmental, diagenetic, and eustatic controls on the permo-triassic carbonate-evaporite reservoir quality, upper dalan and kangan formations, lavan gas field, zagros basin. Geol. J. 53 (4), 1442–1457.
Jarvie, D.M., 2012. Shale resource systems for oil and gas: Part II-Shale-oil resource systems. In: Breyer, J.A. (Ed.), Shale Reservoirs - Giant Resources for the 21st Century, vol. 97. AAPG Mem, pp. 89–119.
Jarvis, I., Mabrouk, A., Moody, R.T.J., Murphy, A.M., Sandman, R.I., 2008. Applications of carbon isotope and elemental (Sr/Ca, Mn) chemostratigraphy to sequence analysis: sea-level change and the global correlation of pelagic carbonates. In: Salem, M.J., El-Hawat, A.S. (Eds.), Geology of East Libya. Earth Science Society of Libya, Tripoli, pp. 369–396.
Jarvis, I., Murphy, A.M., Gale, A.S., 2001. Geochemistry of pelagic and hemipelagic carbonates: criteria for identifying systems tracts and sea-level change. J. Geol. Soc. Lond. 158 (4), 685–696.
Jenkyns, H.C., 2010. Geochemistry of oceanic anoxic events. G-cubed 11 (3), Q03004.
Klemme, H.D., Ulmishek, G.F., 1991. Effective petroleum source rocks of the world: stratigraphic distribution and controlling depositional factors. AAPG Bull. 75 (12), 1809–1851.
Kolodzie, S., 1980. Analysis of pore throat size and use of the Waxman-Smits equation to determine OOIP in Spindle Field, Colorado. Dallas, Texas, USA. In: Proceedings Society of Petroleum Engineers, 55th Annual Technical Fall Conference. SPE-9382-MS.
Langford, F.F., Blanc-Valleron, M.M., 1990. Interpreting Rock-Eval pyrolysis data using graphs of pyrolizable hydrocarbons vs. total organic carbon. AAPG Bull. 74 (6), 799–804.
Latief, A.I., Syofyan, S., Ab Hamid, T.M.T., Al Amoudi, M.A., Shabibi, T.A., 2019. Unlocking tight carbonate reservoir potential: geological characterization to execution. In: SPE Middle East Oil and Gas Show and Conference. Manama, Bahrain. March 18-21. SPE-194712-MS.
Leila, M., Sen, S., Abioui, M., Moscariello, A., 2021. Investigation of pore pressure, in-situ stress state and borehole stability in the West and South Al-Khilala hydrocarbon fields, Nile Delta, Egypt. Geomech. Geophys. Geo-energ. Geo-resour. 7 (3), 56.
Lüning, S., Kolonic, S., Belhadj, E.M., Belhadj, Z., Cota, L., Baric, G., Wagner, T., 2004. Integrated depositional model for the Cenomanian-Turonian organic-rich strata in North Africa. Earth Sci. Rev. 64 (1–2), 51–117.
Makky, A.F., El Sayed, M.I., El-Ata, A.S.A., Abd El-Gaied, I.M., Abdel-Fattah, M.I., Abd-Allah, Z.M., 2014. Source rock evaluation of some upper and lower Cretaceous sequences, West Beni Suef concession, Western Desert, Egypt. Egypt. J. Petrol. 23 (1), 135–149.
Mansour, A., Gentzis, T., Wagreich, M., Tahoun, S.S., Elewa, A.M.T., 2020. Short-term sea level changes of the Upper Cretaceous Carbonates: calibration between palynomorphs composition, inorganic geochemistry, and stable isotopes. Minerals 10 (12), 1099.

Maravelis, A., Zelilidis, A., 2010. Organic geochemical characteristics of the late Eocene-early Oligocene submarine fans and shelf deposits on Lemnos Island, NE Greece. J. Pet. Sci. Eng. 71 (3–4), 160–168.
Moustafa, A.R., 2013. Fold-related faults in the Syrian Arc belt of northern Egypt. Mar. Petrol. Geol. 48, 441–454.
Moustafa, A.R., 2008. Mesozoic cenozoic basin evolution in the northern western Desert of Egypt. In: Salem, M., El-Arnauti, A., Saleh, A. (Eds.), 3rd Symposium on the Sedimentary Basins of Libya. The Geology of East Libya, vol. 3. Earth Science Society of Libya, Tripoli, pp. 29–46.
Nobakht, M., Clarkson, C.R., Kaviani, D., 2013. New type curves for analyzing horizontal well with multiple fractures in shale gas reservoirs. J. Nat. Gas Sci. Eng. 10, 99–112. https://doi.org/10.1016/j.jngse.2012.09.002.
Olde, K., Jarvis, I., Ulicný, D., Pearce, M.A., Trabucho-Alexandre, J., Cech, S., Gröcke, D. R., Laurin, J., Švábenická, L., Tocher, B.A., 2015. Geochemical and palynological sea-level proxies in hemipelagic sediments: a critical assessment from the Upper Cretaceous of the Czech Republic. Palaeogeogr. Palaeoclimatol. Palaeoecol. 435, 222–243.
Ozkan, A., Milliken, K.L., Macaulay, C., Johnston, M., Minisini, D., Eldrett, J.S., Bergman, S., Kelley, A., 2013. Influence of primary rock texture, diagenesis, and thermal maturity on Eagle Ford pore systems. Pittsburgh, Pennsylvania. In: Annual Convention and Exhibition. May 19-22. AAPG Search and Discovery Article #90163.
Perez Altamar, R., Marfurt, K., 2014. Mineralogy-based brittleness prediction from surface seismic data: application to the Barnett Shale. Interpretation 2 (4), T255–T271.
Peters, K.E., 2018. Introduction to petroleum geochemistry, 15th Latin America congress on organic geochemistry 'scientific interdisciplinarity in benefit of organic geochemistry. In: Pre-Conference Course. Salvador, Bahia, Brazil. November 4-7.
Peters, K.E., 1986. Guidelines for evaluating petroleum source rock using programmed pyrolysis. AAPG Bull. 70 (3), 318–329.
Peters, K.E., Cassa, M.R., 1994. Applied source rock geochemistry. In: Magoon, L.B., Dow, W.G. (Eds.), The Petroleum System from Source to Trap, vol. 60. AAPG Mem, pp. 93–120.
Qin, J.Z., Liu, B.Q., Guo, J.Y., Liu, J.W., Yu, G.Y., Guo, S.Z., 2004. Discussion on the evaluation standards of carbonate source rocks. Pet. Geol. Exp. 26 (3), 281–286 (in Chinese).
Qiu, Z.J., Zhang, Y.W., Li, G.Y., Liang, D.G., Wu, Q.Z., Wang, Z.M., Liu, J., 1998. Enlightenment from petroleum geology investigation of Tengiz and Yurubchenskoye carbonate oil-gas fields on exploring Giant oil-gas fields in Tarim Basin. Mar. Origin Pet. Geol. 3 (1), 49–56 (in Chinese).
Radwan, A.E., Trippetta, F., Kassem, A.A., Kania, M., 2021. Multi-scale characterization of unconventional tight carbonate reservoir: insights from October oil field, Gulf of Suez rift basin, Egypt. J. Pet. Sci. Eng. 197, 107968.
Sarhan, M.A., Basal, A.M.K., 2020. Total organic carbon content deduced from resistivity-porosity logs overlay: a case study of Abu Roash formation, Southwest Qarun field, Gindi Basin, Egypt. NRIAG J. Astron. Geophys. 9 (1), 190–205.
Sarhan, M.A., Collier, R.E.L., 2018. Distinguishing rift-related from inversion-related anticlines: observations from the Abu Gharadig and gindi basins, western Desert, Egypt. J. Afr. Earth Sci. 145, 234–245.
Sarhan, M.A., 2017a. Seismic-Wireline logs sequence stratigraphic analyses and geologic evolution for the Upper Cretaceous succession of Abu Gharadig basin, Egypt. J. Afr. Earth Sci. 129, 469–480.
Sarhan, M.A., 2017b. Wrench tectonics of Abu Gharadig Basin, western Desert, Egypt: a structural analysis for hydrocarbon prospects. Arabian J. Geosci. 10 (18), 399.
Sarhan, M.A., 2017c. The efficiency of seismic attributes to differentiate between massive and non-massive carbonate successions for hydrocarbon exploration activity. NRIAG J. Astron. Geophys. 6 (2), 311–325.
Sageman, B.B., Murphy, A.E., Werne, J.P., Ver Straeten, C.A., Hollander, D.J., Lyons, T. W., 2003. A tale of shales: the relative roles of production, decomposition, and dilution in the accumulation of organic-rich strata, Middle-Upper Devonian, Appalachian basin. Chem. Geol. 195 (1–4), 229–273.
Salamy, S.P., Al-Mubarak, H.K., Al-Ghamdi, M.S., Hembling, D.E., 2008. Maximum-reservoir-contact-wells performance update: shaybah field, Saudi Arabia. SPE Prod. Oper. 23 (4), 439–443.
Salamy, S.P., Al-Mubarak, H.K., Hembling, D.E., Al-Ghamdi, M.S., 2006. Deployed smart technologies enablers for improving well performance in tight reservoirs-case: shaybah Field, Saudi Arabia. Amsterdam, The Netherlands. In: Intelligent Energy Conference and Exhibition. April 11-13. SPE-99281-MS.
Sen, S., Abioui, M., Ganguli, S.S., Elsheikh, A., Debnath, A., Benssaou, M., Abdelhady, A. A., 2021. Petrophysical heterogeneity of the early Cretaceous Alamein dolomite reservoir from North Razzak oil field, Egypt integrating well logs, core measurements, and machine learning approach. Fuel 306, 121698.
Shalaby, A., Sarhan, M.A., 2021. Origin of two different deformation styles via active folding mechanisms of inverted Abu El Gharadig Basin, Western Desert, Egypt. J. Afr. Earth Sci. 183, 104331.
Tissot, B.P., Welte, D.H., 1984. Kerogen: composition and classification. In: Tissot, B.P., Welte, D.H. (Eds.), Petroleum Formation and Occurrence. Springer, Berlin, Heidelberg, pp. 131–159.
Tissot, B.P., Welte, D.H., 1978. Petroleum Formation and Occurrence. A New Approach to Oil and Gas Exploration. Springer-Verlag, Berlin.
Tyson, R.V., 1995. Bulk geochemical characterization and classification of organic matter: elemental analysis and pyrolysis. In: Tyson, R.V. (Ed.), Sedimentary Organic Matter: Organic Facies and Palynofacies. Springer, Dordrecht, pp. 367–382.
Wei, Li, Tu, J., Zhang, J., Zhang, B., 2017. Accumulation and potential analysis of self-sourced natural gas in the ordovician Majiagou Formation of Ordos Basin, NW China. Petrol. Explor. Dev. 44 (4), 552–562.
Winland, H.D., 1972. Oil accumulation in response to pore size changes, weyburn field, saskatchewan. Amoco Production Research Report F72-G-25, 1–25.
Yang, X., 2020. Characteristics of mesozoic hydrocarbon source rocks and distribution of remaining resources in the western Desert basin of Egypt. Oil Gas Geol. 41 (2), 423–433.
Zobaa, M.K., Oboh-Ikuenobe, F.E., Ibrahim, M.I., 2011. The Cenomanian/Turonian oceanic anoxic event in the Razzak Field, north Western Desert, Egypt: source rock potential and paleoenvironmental association. Mar. Petrol. Geol. 28 (8), 1475–1482.
Zobaa, M.K., Oboh-Ikuenobe, F.E., Ibrahim, M.I., Arneson, K.K., Browne, C.M., Kholeif, S., 2009. The Cenomanian/Turonian oceanic anoxic event in the Razzak #7 oil well, north Western Desert, Egypt: palynofacies and isotope analyses. In: 2009 GSA Annual Meeting, Abstracts with Programs, p. 513. Portland, Oregon, USA.
Zhang, S.C., Liang, D.G., Zhang, D.J., 2002. Evaluation criteria for Paleozoic effective hydrocarbon source rocks. Petrol. Explor. Dev. 29 (2), 8–12.